Universität Bremen

marum
Center for Marine Environmental Sciences
DFG Research Center · Cluster of Excellence
University of Bremen www.marum.de

Universität Bremen **I MARUM I** 28359 Bremen

To

Gerald (Jerry) Dickens

Editor of Climate of the Past

Dr.
Thomas Westerhold
Research Scientist

Leobener Strasse
MARUM building, Room 0220
28359 Bremen – Germany

Telefon +49 421 218 – 65 672
E-Mail twesterhold@marum.de
www www.marum.de

.

Letter to the editor – Authors' response 2 04. September 2015

Dear Jerry,

Herewith we submit the second revision of the manuscript entitled: “Astronomical Calibration of the Geological Timescale: Closing the Middle Eocene Gap”.

Again we like to thank you for your evaluation of the revised manuscript. We appreciate the comments and have added an extra Section 5.4 that deals with the issues of the correlation and offsets between the bulk $\delta^{13}C$ records of ODP Hole 702B and Site 1263.

We hope that our 2nd revised manuscript meets the requirements to be published in *Climate of the Past*.

Sincerely,

Thomas Westerhold, Ursula Röhl, Thomas Frederichs, Steven M. Bohaty, James C. Zachos

Astronomical Calibration of the Geological Timescale: Closing the Middle Eocene Gap

Thomas Westerhold[1], Ursula Röhl[1], Thomas Frederichs[2], Steven M. Bohaty[3], James C. Zachos[4]

[1]MARUM – Center for Marine Environmental Sciences, University of Bremen, Leobener Strasse, 28359 Bremen, Germany

[2]Department of Geosciences, University of Bremen, 28359 Bremen, Germany

[3]Ocean and Earth Science, University of Southampton, National Oceanography Centre, Southampton, SO14 3ZH, UK

[4]University of California, Santa Cruz, California, USA

Correspondence to: twesterhold@marum.de, phone ++4942121865672

Abstract

To explore cause and consequences of past climate change, very accurate age models such as those provided by the Astronomical Time Scale (ATS) are needed. Beyond 40 million years the accuracy of the ATS critically depends on the correctness of orbital models and radio-isotopic dating techniques. Discrepancies in the age dating of sedimentary successions and the lack of suitable records spanning the middle Eocene have prevented development of a continuous astronomically calibrated geological timescale for the entire Cenozoic Era. We now solve this problem by constructing an independent astrochronological stratigraphy based on Earth's stable 405-kyr eccentricity cycle between 41 and 48 million years ago (Ma) with new data from deep-sea sedimentary sequences in the South Atlantic Ocean. This new link completes the Paleogene astronomical time scale and confirms the intercalibration of radio-isotopic and astronomical dating methods back through the Paleocene-Eocene Thermal Maximum (PETM, 55.930 Ma) and the Cretaceous/Paleogene boundary (66.022 Ma). Coupling of the Paleogene 405-kyr cyclostratigraphic frameworks across the middle Eocene further paves the way for extending the ATS into the Mesozoic.

Autor
Gelöscht: reconstructions highly

Autor
Gelöscht: accurac

Autor
Gelöscht: y

Autor
Gelöscht: inevitable

Autor
Gelöscht: The highly accurate astronomical calibration of the geological time scale b

Autor
Gelöscht: accuracy of

Autor
Gelöscht: Astronomical Time Scale (

Autor
Gelöscht:)

1. Introduction

Accurate absolute age determinations are essential for the geologic study of Earth history. In recent decades the age calibration of the Geological Time Scale was revolutionized by the discovery of astronomically driven cycles in both terrestrial and marine sedimentary archives (Hilgen, 2010). Development of cyclostratigraphic records and application of astronomical tuning (Hinnov, 2013) have evolved into powerful chronostratigraphic tools for highly accurate calibration of the Neogene time scale (Lourens et al., 2004), as well as synchronizing the widely used radio-isotopic $^{40}Ar/^{39}Ar$ and U/Pb absolute dating methods (Kuiper et al., 2008). Limits in the accuracy of astronomically calibrated geological time scale (ATS) are a consequence of uncertainties in astronomical solutions (Laskar et al., 2011a; Laskar et al., 2011b; Laskar et al., 2004). Earth's orbital eccentricity, the deviation of Earth's orbit around the sun from a perfect cycle, is widely used for astronomical calibrations (Hilgen, 2010; Hinnov, 2013). Accurate calculations of Earth's short eccentricity cycle, which has an average period of ~100-kyr, are currently reliable back to 50 Ma and most likely will never extend beyond 60 Ma (Laskar et al., 2011b; Westerhold et al., 2012) due to chaotic behavior of large bodies within the asteroid belt. Despite this, the long (405-kyr) eccentricity cycle is stable back to 200 Ma and thus serves as a metronome for basic cyclostratigraphic calibration of time series (Hinnov and Hilgen, 2012; Laskar et al., 2004) in Mesozoic and early Cenozoic time. Beyond the 50 Ma limit for short eccentricity multimillion-year-long geological records (Hinnov and Hilgen, 2012) with a 405-kyr eccentricity cyclostratigraphic framework have to be anchored in absolute time (Kuiper et al., 2008) by very precise radio-isotopic ages from ash layers.

Autor
Gelöscht: , e.g.,

Because controversy exists regarding the accuracy of high-precision radio-isotope dating and astrochronological calibrations in the Paleocene and Eocene (Kuiper et al., 2008; Westerhold et al., 2012) and the exact age of the Fish Canyon Tuff (FCT) standard for $^{40}Ar/^{39}Ar$ dating (Kuiper et al., 2008; Westerhold et al., 2012; Channell et al., 2010; Phillips and Matchan, 2013; Renne et al., 2010; Renne et al., 1998; Rivera et al., 2011; Wotzlaw et al., 2014; Wotzlaw et al., 2013; Zeeden et al., 2014), extension of the highly accurate ATS beyond 50 Ma into the early Cenozoic and Mesozoic time is not possible. What is needed is a calibration of the Geological Time Scale in the Eocene and Paleocene that is independent from radio-isotopic dating uncertainties and unstable components of astronomical solutions. The best approach is to establish a complete stratigraphic framework for the Cenozoic that is based on the identification of the stable 405-kyr eccentricity cycle and is rooted in the Neogene to late Eocene where all components of the orbital solutions are stable and uncertainties in radio-isotopic ages are negligible. The complete stratigraphic framework will show which published absolute ages within the Eocene and Paleocene epochs, particularly the ages of the Paleocene/Eocene (Westerhold et al., 2012; Charles et al., 2011; Hilgen et al., 2010; Westerhold et al., 2007; Westerhold et al., 2009) and Cretaceous/Paleogene boundaries (Kuiper et al., 2008; Hilgen et al., 2010; Dinarès-Turell et al., 2014; Hilgen et al., 2015; Renne et al., 2013; Westerhold et al., 2008), are correct and consistent with radio-isotopic ages (Kuiper et al., 2008; Renne et al., 2013; Renne et al., 1998; Rivera et al., 2011). To date, a complete stratigraphic framework has not been possible due to the lack of well-defined cyclostratigraphic records spanning the middle Eocene (Pälike and Hilgen, 2008).

Herein, we close the middle Eocene gap in orbitally tuned datasets (Aubry, 1995; Pälike and Hilgen, 2008) by developing an integrated stratigraphic framework based on the identification of the stable 405-kyr cycle (Hinnov and Hilgen, 2012) between 41 and 48 Ma using new data from Ocean Drilling Program (ODP) Sites 702 (Leg 114, (Shipboard Scientific Party, 1988)) and 1263 (Leg 208, (Shipboard Scientific Party, 2004)) in the South Atlantic Ocean (Fig. 1). This was achieved by establishing a magnetostratigraphy across magnetic polarity chrons C20r and C21n at Site 1263, then combining this with high-resolution bulk carbon isotope ($\delta^{13}C$) records from Sites 702 and 1263. These new data, together with previously available shipboard stratigraphic data allow us to construct a robust 405-kyr cyclostratigraphic framework across a ~7-Myr window of the middle Eocene.

2. Material and methods

2.1 Study sites

For this study we generated new geochemical and paleomagnetic data on carbonate rich sediments from Ocean Drilling Program (ODP) South Atlantic Site 702 (Leg 114, (Shipboard Scientific Party, 1988)) and Site 1263 (Leg 208, (Shipboard Scientific Party, 2004)) (Fig. 1). ODP Site 702 is located in the southwestern South Atlantic on the central part of the Islas Orcadas Rise (50°56.79'S, 26°22.12'W) in 3083.4 m water depth. In April 1987 only a single hole (Hole 702B) was drilled into Paleogene strata with extended core barrel (XCB) down to 294.3 meters below sea floor (mbsf), recovering a thick sequence of nannofossil ooze and chalk middle Eocene in age (Shipboard Scientific Party, 1988). For this study, samples were analyzed from Hole 702B in the ~90 and 210 mbsf interval (Fig. 2). ODP Site 1263 is located in the southeastern South Atlantic on Walvis Ridge (28°31.97'S, 2°46.77'E) in 2717 m water depth (Shipboard Scientific Party, 2004). At this site, a sequence of Paleogene strata was cored in four adjacent holes that have been combined to a composite record down to 340 meters composite depth (mcd). After revision of the Site 1263 composite record (see below), samples for this study were obtained from the interval between ~150 and 230 revised meters composite depth (rmcd) of 1263 (Fig. 2).

Autor
Gelöscht: section between

2.2 Bulk stable isotope data

Bulk carbonate $\delta^{13}C$ measurements were made in two different labs on freeze-dried and pulverized sediment samples from ODP Sites 702 and 1263. A total of 539 samples from Site 702 were analyzed at University of California Santa Cruz (UCSC) between Sections 702B-11X-1 and 702B-22X-CC at an average sampling resolution of 20 cm (~13 kyr temporal resolution, Table S1, Fig. 2). A total of 1157 samples in total were analyzed from Site 1263 (Table S2, Fig. 2). 668 of these samples spanning mid magnetochron C19r to mid C20r were analyzed at MARUM, University of Bremen, with an average resolution of 4 cm (5 kyr). The remaining 489 samples from Site 1263 spanning mid C20r to base C21r were measured at UCSC with average resolution of 10 cm (10 kyr). All $\delta^{13}C$ data are reported relative to the Vienna Pee Dee Belemnite (VPDB) international standard, determined via adjustment to calibrated in-house standards and NBS-19. Analyses at MARUM were carried out on a Finnigan MAT 251 mass spectrometer equipped with an automated carbonate preparation line (Kiel I). The carbonate was reacted with orthophosphoric acid at 75 °C. Analytical precision based on replicate analyses of in-house standard (Solnhofen Limestone) averages 0.04‰ (1σ) for $\delta^{13}C$. Stable isotope analyses at UCSC were performed on VG Prism and Optima dual-inlet

Autor
Gelöscht: processed

mass spectrometers coupled with Autocarb automated preparation devices in which the samples are reacted using a carousel device and common acid bath maintained at 90 °C. Analytical precision based on replicate analyses of an in-house Carrara Marble standard and NBS-19 averaged 0.05‰ (1σ) for $\delta^{13}C$.

2.3 Paleomagnetic data Site 1263

We measured natural remanent magnetization (NRM) on 100 discrete cube samples (gauge 2cm×2cm×2cm) to document magnetic polarity boundaries C19r to C21r at ODP Site 1263. Discrete samples were analyzed at the Department of Geosciences, University of Bremen. Paleomagnetic directions and magnetization intensities were measured on a cryogenic magnetometer (model 2G Enterprises 755 HR). NRM was measured on each sample before these were subjected to a systematic alternating field demagnetization treatment involving steps of 7.5, 10, 15, 20, 25, 30, 40 and 60 mT. Intensities of orthogonal magnetic components of the remanent magnetization were measured after each step. Raw inclination, declination, and intensity data for each measurement step are provided in Table S3, and the magnetostratigraphic interpretations are recorded in Table S4.

Autor
Gelöscht: is

2.4 Time series analysis

To investigate Milankovitch-paced cyclicity in our datasets, we calculated evolutionary spectra in the depth and time domain to identify the dominant cycle periods and to detect distinct changes in these cycle periods. In order to obtain a first-order age model unaffected by astronomical tuning, we applied the magnetostratigraphy available for Sites 702 (Clement and Hailwood, 1991) and 1263 (this study, Table S3) using the Geomagnetic Polarity Time Scale of (Cande and Kent, 1995). Wavelet analysis was used to compute evolutionary spectra using software provided by C. Torrence and G. Compo (available online at http://paos.colorado.edu/research/wavelets). Prior to wavelet analysis the data were detrended and normalized. Multitaper Method (MTM) spectra were then calculated with the SSA-MTM Toolkit (Ghil et al., 2002) using 3 tapers and resolution of 2. Background estimate and confidence levels (90%, 95%, and 99%) are based on robust red noise estimation (Mann and Lees, 1996). Prior to analysis outliers and the long-term trend were removed, and the time series was linearly resampled at 4-kyr (Site 702) and 2-kyr (Site 1263) intervals. After identification of the frequency and period of the short and long eccentricity-related cycles in the bulk $\delta^{13}C$ data of both study sites, the 405-kyr cycle was extracted by band-pass filtering.

3. Results

All data are available online at http://doi.pangaea.de/10.1594/PANGAEA.845986.

3.1 Revised composite record for ODP Site 1263

In order to ensure a fully complete stratigraphic record at Site 1263 we checked the shipboard composite record using shipboard magnetic susceptibility data and digital line scan high-resolution core images (Fig. S1). Small changes in the order of cm to a few dm were applied to optimize the splice and avoid coring induced disturbance in the isotope data. A major change had to be made around 120 rmcd which was reported as problematic during shipboard analysis (Shipboard Scientific Party, 2004). Core 1263C-2H was moved downwards by 2.52 m to match the base of Core 1263B-6H. Core 1263B-7H was then re-correlated to Core 1263C-7H by moving the core 3.34 m downward. Although this tie is difficult due to core disturbance the core images provided a good reference. This tie does not affect the record presented in this study because it is located at 125 rmcd and will be re-evaluated by additional bulk isotope data in the future. The composite splice was revised here down to 229.22 rmcd. Below this level, there is strong drilling disturbance across a 3–4-m interval. For completeness we report the full composite splice and offsets applied to adjust each core for Site 1263 in Table S7 and S8.

3.2 Magnetostratigraphic results and interpretation

A detailed vector analysis according to the method by Kirschvink (Kirschvink, 1980) without anchoring to the origin of the orthogonal projections was applied to the results of the AF demagnetization of NRM to determine the characteristic remanent magnetization

(ChRM). Additionally the maximum angular deviation (MAD) values were computed reflecting the quality of individual magnetic component directions. MAD values are all below 10 degree (Figure 3).

Figures 3b and 3c display the demagnetization characteristics of a sample with reversed polarity from C19r and a sample with normal polarity from C21n, respectively. As an example for samples with demagnetization behavior with larger scatter (larger MAD), data from a sample within C21r is plotted in Figure 3d. The larger MADs that a few samples show are not simply related to the intensity of their remanent magnetization as can be seen from the data shown in Figure 3. The median destructive field (MDF) of the NRM demagnetization is comparable low for most of the samples. It ranges from 4 to 24 mT (mean 7.1 +/- 4.1 mT) indicating a magnetically soft overprint in many samples. The interpretation of the ChRM in terms of magnetic polarity is focused on the inclination data, which provides a reliable magnetostratigraphy for most intervals. Identification and position of calcareous nannofossil events in 702B (Pea, 2011) and 1263 (Shipboard Scientific Party, 2004) (Fig. 2; Table S5) allow to clearly identify the magnetic chrons as C19r, C20n, C20r, C21n and C21r. Raw inclination, declination, and intensity data for each measurement step for ODP 1263 are given in Table S3. Magnetostratigraphic interpretation is given in Table S4. Processed paleomagnetic data from ODP 1263 basis for the magnetostratigraphic interpretation are provided in Table S9.

3.3 Bulk stable isotope results

The bulk carbon stable isotope data of Hole 702B (Fig. 2a) show a long-term increase from 0.8 to 2.0 ‰ in the interval Chron C21r to C18r. Site 1263 data (Fig. 2b) reveal a decrease from 2 to 1.6 ‰ from Chron C21r to C21n, an increase from 1.6 to 2 ‰ across the C20r/C21n boundary, a slight increase to 2.2 ‰ in the interval covering the mid Chron C20r to C20n, a decrease of 0.2 ‰ in Chron C20n, and an increasing trend in the early Chron C19r. The shift in carbon isotope data across the C20r/C21n boundary and the decrease in Chron C20n is very similar in both records pointing to global changes in the global carbon cycle. Both records show pronounced higher frequency variations related to short (100 kyr) and long (405 kyr) eccentricity cycles (see below).

4. Age Model development

The age model for Sites 702 and 1263 was developed in a progressive series of steps. First, time series analysis was applied to the bulk $\delta^{13}C$ data from both Sites 702 and 1263 using evolutionary wavelet (Fig. 4) and MTM power spectra (Fig. S2 & S3). The Site 702 $\delta^{13}C$ record is dominated by 6-8 m and ~2 m cycles, whereas Site 1263 is dominated by 3.5-4.5 m and ~1 m cycles. Conversion to age applying the Geomagnetic Polarity Time Scale (GPTS) CK95 (Cande and Kent, 1995) reveals that these cycles correspond to the short (~100-kyr) and long (405-kyr) eccentricity periods – similar to observations in early (Zachos et al., 2010) and late Eocene (Westerhold et al., 2014) deep-sea sediments.

Second, the dominant 405-kyr related cycles were extracted by band-pass filtering at the appropriate interval (Fig. 5; Site 702: 0.16 ± 0.048 cyc/m; Site 1263: 155-180 rmcd 0.29 ± 0.087 cyc/m, 180-230 rmcd 0.23 ± 0.069 cyc/m). After correlating the Site 702 and 1263 records via magneto-stratigraphic tie points, a relative floating 405-kyr age model was established by counting cycles starting with 1 in the Site 1263 record at 158.60 rmcd (Tab. S6). We determine a 2.6 to 2.7-Myr duration for magnetochron C20r and a 1.4-Myr duration for magnetochron C21n. Our new estimate for the duration of C20r is consistent with estimates from the standard CK95 (Cande and Kent, 1995) and GPTS2004 (Ogg and Smith, 2004) as well as a previous cyclostratigraphic estimate from the Contessa Highway section in Italy (Jovane et al., 2010), but is ~400 kyr shorter than that estimated within the GPTS 2012 time scale (Ogg, 2012; Vandenberghe et al., 2012) (Fig. 5, Tables 1-2).

Third, the floating 405-kyr age model was connected to the astronomical time scale (ATS) by correlation to ODP Site 1260 (Westerhold and Röhl, 2013; Westerhold et al., 2014) over magnetochron C20n (Fig. 6a). Site 1260 is tied to the cyclostratigraphic framework for the late middle Eocene-to-early Oligocene interval (Westerhold et al., 2014) and therefore establishes an independent bridge between the astronomically calibrated time scales of the Neogene to late Eocene and early Paleogene. The correlation and calibration of the cyclostratigraphic records from Sites 702 and 1263 place the boundary of magnetochron C20n/C20r in 405-kyr Cycle 108 (43.5 Ma), the C20r/C21n boundary between 405-kyr Cycle 114 and 115 (~46.2 Ma), and the C21n/C21r boundary in 405-kyr cycle 118 (~47.6 Ma) (Fig. 5; Tables 1-2).

Fourth, because the orbital solutions La2010d and La2011 are valid back to ~50 Ma and the pattern of long and very long eccentricity cycle related components in both the Site 702 and 1263 bulk $\delta^{13}C$ records are very consistent with the La2010d and La2011 orbital solution for eccentricity, the carbon isotope records were minimally tuned to the La2011 eccentricity by correlating lighter (more negative) $\delta^{13}C$ peaks to eccentricity maxima (Fig. 5, (Ma et al., 2011)). This phase relationship has been observed in other deep-sea $\delta^{13}C$ bulk and benthic records (Pälike et al., 2006; Westerhold et al., 2014; Zachos et al., 2010) and thus is used here for the foundation of the tuning method (see supplementary material). The tie points to establish an astronomically tuned age model are shown in Fig. 5 and listed in Table S10.

A potential issue in establishing a 405-kyr-based cyclostratigraphy is the missing or doubling of a 405-kyr cycle. Because the band-pass filter at Cycle 10 at Site 1263 shows a conspicuous cycle with a double hump (Fig. 5) and a stretched Cycle 9 at Site 702, we also provide an alternative 405-kyr age model with one additional 405-kyr cycle (18 instead of 17 for the investigated interval of this study). Sedimentation rates calculated based on the 17 cycles-, the 18 cycles-, the magnetostratigraphic (using CK95) and the astronomical age model show a distinct drop using the 18 cycles model with respect to the other models (Fig. S5). Choosing the 18 cycles model would therefore lead to an unrealistically long duration for Chron C20r of more than 3.0 myr. In addition, the orbital solutions La2010d and La2011 are valid back to ~50 Ma and thus the match between the geological record and the astronomical solution as far as the expression of the 2.4 myr minima provides an important argument for rejecting the presence of a potential extra 405-kyr cycle (Fig. 5). Based on these arguments we discarded the 18 405-kyr cycles model as an option.

Autor
Gelöscht: S4

By connecting the astronomically calibrated Site 1263 $\delta^{13}C$ record with the geochemical records of ODP Sites 1258 and 1262 we can extend the ATS into the early Paleogene up to the Cretaceous/Paleogene (K/Pg) boundary based on a continuous 405-kyr cyclostratigraphic framework. This not only allows for comparison of the eccentricity related components in the geochemical records to the recent orbital solutions La2010 and La2011, but also provides accurate absolute ages for ash -17, the Paleocene-Eocene Thermal Maximum (PETM) and the K/Pg boundary independent from radio-isotopic dating and uncertainties in the 100-kyr and 2.4 myr eccentricity cycle components. Using bulk and benthic $\delta^{13}C$ records as well as magnetostratigraphy, Site 1258 (Sexton et al., 2011) and Site 1263 (this study) can be tied together at 405-kyr Cycles 118 and 119 over the magnetochron C21n/C21r boundary (Fig. 6b). This establishes the connection of the early Paleogene cyclostratigraphies with the ATS of the Neogene and late Paleogene where all components of the orbital solutions are stable and uncertainties in radio-isotopic ages are very small. Closing the middle Eocene cyclostratigraphic gap establishes a complete and fully astronomically calibrated geological timescale for the Cenozoic and is the basis for extending the ATS into the Mesozoic.

5. Discussion

Integration of new and previously published results from ODP Sites 1258, 1260, 1262, and 1263 allows (i) placement of these records on a common 405-kyr cycle astronomically calibrated time scale across the middle Eocene, and (ii) evaluation of the evolution of Earth's eccentricity in the context of the latest generation of astronomical models for intervals older than 50 Ma.

5.1 Consistent absolute ages for the Paleogene

To assemble a complete Eocene GPTS, we combined the GPTS of the Pacific Equatorial Age Transect (PEAT, 31-41 Ma, C12n to C19n, (Westerhold et al., 2014)), of Site 1260 (41-43 Ma, C19n to C20n, (Westerhold and Röhl, 2013)), of Site 1263 (42-48 Ma, C20n-C21n, this study), and of Site 1258 (48-54 Ma, C21n-C24n, (Westerhold and Röhl, 2009)) and updated to the age model established in this study (Tab. S11 & S12, Fig. 7).

The resulting Eocene GPTS covers magnetochron C12n to C24n and together with the recalibrated early (C29n to C27n, (Dinarès-Turell et al., 2014)) and late Paleocene (C26 to C24r, Option 2 in (Westerhold et al., 2008)) as well as Oligocene (C6Cn to C12n, (Pälike et al., 2006)) it provides a full GPTS for the Paleogene period. The new tuned GPTS and the GPTS2012 (Ogg, 2012; Vandenberghe et al., 2012) are nearly consistent. Differences with respect to GPTS2012 are apparent for the duration of C20r, C22r and C23n.2n (Fig. 7A). The 2.634 myr duration for C20r interpreted in this study is consistent with estimates from the standard CK95 GPTS (Cande and Kent, 1995) and GPTS2004 (Ogg and Smith, 2004) as well as a previous cyclostratigraphic estimate from the Contessa Highway section in Italy (Jovane et al., 2010). The difference for the duration of C20r to the estimate in GPTS2012 could be related to the selection of tie points for calibration of the GPTS. In GPTS2012 the astronomic age model with 6-order polynomial fit in the Eocene and the radio-isotopic age model give an absolute age for the top of C22n of 49.102 Ma and 48.570 Ma, respectively (Table 28.3 therein (Vandenberghe et al., 2012)). This difference of 536 kyr mirrors the uncertainty in this interval of the time scale GPTS2012. However, the radio-isotopic ages are primarily used for the final age model in GPTS2012 from C16r to the top of C24n.1n (37-53 Ma, (Vandenberghe et al., 2012)). GPTS2012 uses the Mission Valley ash near the base of C20n with $^{40}Ar/^{39}Ar$ age of 43.35 Ma which is consistent with our tuned age of 43.517 Ma for the base of C20n. Because of the relatively large error in the next calibration point (an ash horizon in DSDP Hole 516F at C21n.75 with an age of 46.24±0.5 Ma (Vandenberghe et al., 2012)) the duration of C20r in GPTS2012 (2.292 myr) has to be considered with caution. The differences in duration of C22r and C23n.2n (~400-kyr longer C22r; ~400-kyr shorter C23n.2n) could be related to the difficult interpretation of the Site 1258 magnetostratigraphy (Westerhold and Röhl, 2009) and require recovery of additional high-quality records from deep-sea successions in the future for confirmation. This uncertainty in the duration of C22r and C23n.2n at Site 1258 does not affect the number of 405-kyr cycles identified in this record, but is the result of uncertainties in determining the exact position of the magnetic reversal. This is complicated by the rather large error in the width of the magnetic anomaly profiles for C21r (12.8%), C22r (11.9%) and C23 (17.3%) (Cande and Kent, 1992; Tab. 4 therein) which results in very uncertain

Autor
Gelöscht: in

chron durations (see Table S13). Combining both the error in absolute age for the calibration tie points (ash layers, boundaries) and the error in the exact placement of boundaries between marine magnetic anomalies in the CK95 model (Table S13) it is obvious that the determination of the exact durations of magnetochrons is much more difficult than assumed in many publications. Once the durations for C21r, C22r and C23 based on the ODP Site 1258 cyclostratigraphy are evaluated by an additional high-resolution bio-,magneto- and cyclostratigraphy on another site, the resulting new precise cycle-durations for chrons could help to provide an improved estimate for the deep-seas magnetic anomaly widths as in CK95.

Previous correlation of geological data to the La2011 orbital solution led to a discrepancy between astronomical and radio-isotopic $^{40}Ar/^{39}Ar$ ages of ash -17 (Storey et al., 2007) derived from Deep Sea Drilling Project (DSDP) Site 550 (Knox, 1984) and the age of the Paleocene-Eocene Thermal Maximum (PETM) (Vandenberghe et al., 2012; Westerhold et al., 2012; Westerhold et al., 2009). Linking the published cyclostratigraphies for the Paleocene (Westerhold et al., 2008) and early to middle Eocene (Westerhold and Röhl, 2009; Westerhold et al., 2012; Westerhold et al., 2007) to our ATS across the C21n/C21r boundary in 405-kyr Cycle 118 at ~47.6 Ma (Fig. 6b) clearly shows that only Option 2 (Westerhold et al., 2012; Westerhold et al., 2007) of the early-to-middle Eocene floating cyclostratigraphies is consistent with our new astronomically tuned age for C21n/C21r boundary. Our records spanning the middle Eocene cyclostratigraphic gap provide an absolute age estimate of 55.280 Ma for ash -17 and the onset of the PETM in 405-kyr Cycle 139 at 55.930 Ma, as in Option 2 of the astronomically calibrated Paleocene time scale (Westerhold et al., 2008). This age for the onset of the PETM is consistent with a high-precision radio-isotopic U/Pb age of 55.728–55.964 Ma from bentonite layers within the PETM interval at Spitzbergen (Charles et al., 2011). The absolute age for the onset of the PETM confirmed here at 55.930 Ma is also synchronous with the initiation of North Atlantic flood basalt volcanism (Skaergaard intrusion at 55.960 ± 0.064 Ma, (Wotzlaw et al., 2012)).

After revision of the Paleocene cyclostratigraphy from deep-sea data (Dinarès-Turell et al., 2014) showing that the Paleocene spans 25 (Hilgen et al., 2010) and not 24 (Westerhold et al., 2008) 405-kyr cycles and with the complete stratigraphic framework now at hand we provide absolute astronomical ages for key events in the Eocene and Paleocene for reference (Table 3). Updates for ages of magnetochron boundaries await solving the uncertainties for the durations of Chrons C22n to C23r. Our complete framework confirms the astronomically calibrated age of the K/Pg boundary of 66.022 ± 0.040 Ma (Dinarès-Turell et al., 2014). This is consistent with a recent high-precision radio-isotopic U/Pb age for the K/Pg boundary of 66.038 Ma (Renne et al., 2013). The major uncertainty in age estimates stems from uncertainties in the exact absolute age assignment of the 405-kyr eccentricity maxima at 56 and 66 Ma. According to (Laskar et al., 2011a; Laskar et al., 2011b) the error at 56 Ma is in the order of 50 kyr and at 66 Ma in the order of 60 kyr.

The astronomically calibrated age for ash -17 of 55.280 Ma is inconsistent with $^{40}Ar/^{39}Ar$ ages using the most recent age calibrations for the FCT dating standard monitor of 28.201 (Kuiper et al., 2008), 28.305 (Renne et al., 2010), 27.93 (Channell et al., 2010), 27.89 (Westerhold et al., 2012), and 28.172 (Rivera et al., 2011) Ma (Fig. S7). Assuming that the 55.280 Ma age for ash -17 is correct we calculate an absolute age of ~28.10 Ma for the FCT monitor which is within the error of the 28.172 (Rivera et al., 2011) Ma estimate. The age of 28.10 Ma for the FCT leads to an age for the highly reproducible inter-laboratory $^{40}Ar/^{39}Ar$ measurements made on the Beloc tektite at the K/Pg boundary that is more than 400 kyr younger than the highly accurate U/Pb age (Renne et al., 2013) contradicting the rock clock synchronization (Kuiper et al., 2008). Independent confirmation of the ~28.2 Ma astronomically calibrated age for the FCT (Kuiper et al., 2008; Rivera et al., 2011; Wotzlaw et al., 2014) and the absolute age of the K/Pg boundary of 66.022 Ma (Dinarès-Turell et al., 2014; Kuiper et al., 2008; Renne et al., 2013) place doubt on the astronomically calibrated age for ash -17. Both the geochemical identification of ash -17 in ODP Site 550 (Knox, 1984) and the relative distance to the onset of the PETM (Westerhold et al., 2009) need revision before any evaluation can be done.

5.2 Terrestrial vs deep-sea GPTS

Autor
Gelöscht: age

Autor
Gelöscht: 6

High-resolution radio-isotopic dating of Eocene terrestrial strata, from the Green River Formation in particular, has been utilized during the last 20 years towards improving the Eocene GPTS (Clyde et al., 2004; Clyde et al., 2001; Clyde et al., 1997; Machlus et al., 2004; Machlus et al., 2008; Machlus et al., 2015; Shipboard Scientific Party, 1988; Smith et al., 2008a; Smith et al., 2008b; Smith et al., 2010; Smith et al., 2003; Smith et al., 2006; Smith et al., 2004; Tsukui and Clyde, 2012; Westerhold and Röhl, 2009). Although one must state that the correlation of terrestrial sections and accurate age dating of ash layers is highly complex we evaluate our new GPTS in comparison with to the terrestrial calibrations (Fig. 7a). Focusing on the latest Green River Formation GPTS calibrations (all adjusted and reported by Smith et al. (2010) and Tsukui & Clyde (2012) to FCT 28.201 Ma of Kuiper et al. (2008)), it becomes very clear that substantial differences in calibration and interpretation exist that are based on very similar data sets.

Because most of the radio-isotopic dates for ash layers in the Green River Formation are established on $^{40}Ar/^{39}Ar$ ages, they are directly dependent on the absolute age of the FCT standard (see discussion in Westerhold & Röhl (2009) and Westerhold et al. (2012)). High quality U/Pb ages are also available for some ash layers (Smith et al. 2010 [Analcite and Firehole tuff] and Machlus et al. 2015 [Sixth, Layered, Main, Grey, Second, Firehole and 1448 Tuff]). The Firehole tuff has a consistent U/Pb age of 51.66 ± 0.19 Ma in Smith et al. (2010) and 51.528 ± 0.061 Ma in Machlus et al. (2015). The $^{40}Ar/^{39}Ar$ age of the Firehole Tuff is 51.40 ± 0.25 Ma (FCT 28.201 Ma) (Smith et al. 2010). The Firehole tuff, however, was not included by Smith et al. (2010) for recalibrating the GPTS. According to Tsukui & Clyde (2015) the Firehole tuff is in a paleomagnetic reversal, likely C23r (see Table DR4 in Tsukui & Clyde 2012). Unfortunately, the Analcite Tuff (U/Pb 49.23 ± 0.12 Ma, Smith et al. 2010) has not clear paleomagnetic polarity (Tsukui & Clyde 2015). Comparing the radioisotopic ages used by Smith et al. (2010) and their paleomagnetic pattern with the astronomically calibrated GPTS (Fig. 7a) shows consistent results for the Mission Valley ash (in C20n), the Montanari ash (in C21n), the Blue Point Marker ash (in C21r), the Continental tuff (in C22n), the Firehole tuff (in C23r) and the Willwood ash (in C24n). Inconsistencies are apparent for the Sixth tuff and Layered tuff which have normal polarity but correlate to C22r in the astronomical GPTS.

Tsukui & Clyde (2012) utilized more ash layers for their calibration that has substantial differences to the GPTS by Smith et al. (2010) from C21n to C24n (Fig. 7b). Some ash layers, for example, in C21r and C23n of the GPTS of Tsukui & Clyde (2012), have opposite polarities although they are of similar age. The GPTS of Tsukui & Clyde (2012) is more consistent with the astronomical GPTS for Chron C22 and C23, but the Sixth ash, the Layered tuff and the Main tuff occur in an interval of normal polarity correlate to C22r in the astronomical GPTS. In contrast, the Firehole tuff, located in an interval of reversed polarity, is positioned in C23n according to the GPTS of Tsukui & Clyde (2012). We would argue that the duration of C23n as estimated by Tsukui & Clyde (2012) is probably too long. A detailed comparison of the GPTS for Chrons C22 and C23 between terrestrial and deep-sea records is difficult at the moment because the deep-sea and the terrestrial GPTS still need to be examined in detail in the early Eocene, as described above. The error in the mean width of the anomaly profile defined by Cande and Kent (1992, Table 4 therein) for C21r, C22r and C23 is between 12 and 17% (Table S13), which can also help to explain larger differences in durations between the terrestrial and deep-sea records. A new deep-sea magneto-cyclostratigraphic record is needed to test the ODP Site 1258 results in order to validate the duration of magnetochrons C22 and C23. Nevertheless, it seems that these records align for Chron C24n suggesting that both astrochronology and radio-isotopic dating of terrestrial successions are in agreement for at least this time interval. A more detailed comparison between marine and terrestrial records is well beyond the scope of this paper, a more in-depth synthesis and discussion of terrestrial and deep-sea GPTS for the Eocene has to be addressed by a future synthesis similar to the Paleogene chapter in the GTS2012 (Vandenberghe et al., 2012).

5.3 Stability of orbital solutions

The new $\delta^{13}C$ records from Sites 702 and 1263 reveal low amplitude variations in 405-kyr cycles 4, 10 and 16 (Fig. 5), which likely coincide with minima in eccentricity amplitude modulation occurring approximately every 2.4 Myr (Laskar et al., 2004). The 2.4-Myr cycle in the amplitude modulation of geological data and orbital eccentricity are consistent up to 48–49 Ma (Fig. S6). In older time intervals, the geological data and

Autor
Gelöscht: 5

orbital solution are out of sync suggesting that the short and very long eccentricity component in orbital solutions are correct only back to 48 Ma, but not to 52-54 Ma as previously thought (Westerhold et al., 2012). This implies that only the stable 405-kyr eccentricity pattern in the La2010 and La2011 solutions can be used for direct astronomical calibration for periods older than 48-50 Ma. Because the orbital solutions La2010d and La2011 (Laskar et al., 2011a; Laskar et al., 2011b) show an excellent fit to the internally-anchored $\delta^{13}C$ records the long-term behavior of the INPOP10a (Intégration Numérique Planétaire de l’Observatoire de Paris, (Fienga et al., 2011)) ephemeris used for La2010d and La2011 can be considered more stable than that of the INPOP08 (Fienga et al., 2009) ephemeris.

The divergence between geological data and astronomical solutions beyond 48-50 Ma has strong implications for the La2010 (Laskar et al., 2011a) and La2011 (Laskar et al., 2011b) orbital models. Both models propose a transition from libration to circulation appearing around 50 Ma in the resonant argument related to $\theta = (s4 - s3) - 2(g4 - g3)$, the combination of angles in the precession motion of the orbits of Earth and Mars (Laskar et al., 2004; Pälike et al., 2004). Identifying this transition is of high importance because it would provide direct evidence of the chaotic, not quasiperiodic, nature of the solar system (Laskar, 1989) and set the conditions for the gravitational model of the Solar System (Laskar et al., 2004). In modern planetary ephemeris the initial conditions are obtained by least-squares fittings to large sets of observational data (Fienga et al., 2008) and thus depend on the accuracy of these data. The point in time when the transition from libration to circulation occurs is sensitive to the initial conditions of the planetary ephemeris solutions. In geological records the chaotic diffusion will be expressed as a prominent change from a ~2.4-Myr to a very regular 2.0-Myr periodicity in the very long eccentricity cycle (Laskar et al., 2004; Pälike et al., 2004). Due to irregular spacing from 4 to 6 long eccentricity cycles between very long eccentricity minima in the geological data from 50 to 60 Ma the chaotic diffusion of the orbital trajectories as proposed in La2010d and La2011 cannot be verified (Fig. S6). This major discrepancy points to inaccuracy in the planetary ephemeris solutions, which are currently limited due to the chaotic behavior of the large asteroids (Laskar et al., 2011b). The transition from libration to circulation needs to be identified in older geological intervals to help to refine orbital

Autor
Gelöscht: 5

models. A precise calculation of Earth's eccentricity beyond 60 Ma is not possible (Laskar et al., 2011b) but geological data, preferably stable carbon isotope data, from 50 to 100 Ma could help to detect this critical transition and provide important information for future orbital models.

Autor
Gelöscht: e.g.

5.4 Comparing the bulk carbon isotope records from 702B and 1263

One might recognize an interesting aspect of aligning $\delta^{13}C$ curves at two sites. Given all the factors that influence seawater carbon isotopes and carbonate production and deposition, there is no a priori reason to assume that bulk sediment $\delta^{13}C$ should co-vary in records across the ocean basins, and yet they often do, and therefore these patterns are used for chemostratigraphy (Cramer et al., 2003; Zachos et al., 2010; Littler et al. 2014M; Saltzman and Thomas 2014). However, the observation that mean $\delta^{13}C$ values deviate between sites and especially on long time scales should not come as a surprise, especially as ocean circulation is shifting and biota are evolving. The challenge is to extract the orbital patterns for stratigraphic purposes from these records, the relative modulation of which should be similar, even as the means deviate. The Oligocene-Miocene records provide good examples where the 405-kyr cycles can be extracted and correlated even as mean values deviate between records (Zachos et al., 2001; Pälike et al., 2006; Holbourn et al., 2013).

The $\delta^{13}C$ records in our study do correlate between 41.5 and 44.5 Ma with similar absolute bulk $\delta^{13}C$ values and similar trends/orbital-scale cyclicity. Between 44.5 and 47 Ma Site 702 is offset relative to Site 1263 by 0.3-0.4‰ (Fig. 5a), but trends and overall patterns of orbitally-paced events are similar. In the 47 to 49 Ma interval offset values and trends are different, but the pattern with a double $\delta^{13}C$ excursion at ~48 Ma is the same. The mismatch around 47.5 Ma could indicate a potential unidentified hiatus between 47 and 48 Ma in one of the sites. Please note that despite the offset from 44.5 to 49 Ma both $\delta^{13}C$ curves show a very similar trend from 45.5 to 47 Ma including the minimum in amplitude modulation at eccentricity 405-kyr cycle 113. In supplementary Figure S8 both records are plotted on the same as well as on separate $\delta^{13}C$ axes to demonstrate the coherently corresponding pattern of both records. This clearly exhibits that the chronostratigraphy between sites is consistent and therefore correct. The offset from 44.5 to 48 Ma is only impeding the visual comparison.

In contrast, a somehow problematic interval lies between 47 and 48 Ma, where the bulk isotope data exhibit both offset trends and values. The two peaks in Hole 702B bulk $\delta^{13}C$ data at 47.39 and 47.55 Ma (see Fig. S8) are based on single measurements and therefore should not be over-interpreted, e.g. as $\delta^{13}C$ excursions or even (mis)used for direct value-to-value correlation to 1263. The $\delta^{13}C$ excursion seen at Site 1263 at 47.2 Ma is not well expressed in Hole 702B bulk data. But, the cyclostratigraphy for this Site 1263 interval is straightforward because the 405-kyr cycles can be clearly identified (Fig. 5, cycles 14-16). 405-kyr cycles 14 and 15 are hard to assign in Hole 702B, but cycle 16 can and it also correlates to cycle 16 at Site 1263 with the prominent double $\delta^{13}C$ peaks at 48.0 and 48.1 Ma. Cycle 16 is located in C21r in both records and thus we can be confident that there is no major gap in the Hole 702B record.

Finally, there might be an interesting divergence in the $\delta^{13}C$ of surface waters in the south Atlantic during the middle Eocene assuming the bulk $\delta^{13}C$ signal at Hole 702B and Site 1263 mainly comes from coccolith and planktonic foraminiferal carbonate. The stratigraphic pattern seems consistent between Sites 702 and 1263, therefore we interpret the observed divergence and offset in the $\delta^{13}C$ signal as a result of changes in the surface water at Site 702. Site 1263 is from the middle of the South Atlantic gyre and Site 702 from higher latitude on the edge of the gyre. It might be that differences in surface-water nutrient levels or/and stratification existed. Even though both sites are comprised of slowly accumulated pelagic carbonates, Site 702 would likely have been subject to higher nutrient conditions and/or more variability in nutrient supply, as for example indicated by biogenic silica (radiolarians, silicoflagellates) in the upper middle Eocene section of Site 702. The lower bulk $\delta^{13}C$ values in the older part of the record at Site 702 could be indicative of higher nutrient levels or a deeper depth of production of calcareous nannoplankton. Given all the variables that control mixed-layer $\delta^{13}C$-DIC (including also air-sea CO_2 exchange) the two sites should not really be expected to have similar bulk $\delta^{13}C$ values. Low-resolution benthic $\delta^{13}C$ data from Hole 702B (Katz and Miller, 1991;

Fig. S8) show a possible 0.2‰ shift at ~44.5 Ma pointing towards changes in surface and deep ocean carbon signatures. The similar pattern in bulk $\delta^{13}C$ data of Sites 702 and 1263 suggests that both sites are recording the primary signal and it is very unlikely that diagenetic alteration affected the signal at both sites the same way. The shift in bulk $\delta^{13}C$ data at 44.5 Ma does not influence the stratigraphic interpretation but might be a very interesting feature for further paleoceanographic investigations.

6 Conclusions

The closing of the middle Eocene gap and the connection of the 405-kyr cyclostratigraphies of the Eocene and Paleocene complete a fully astronomically calibrated geological timescale for the Cenozoic. Derived absolute ages for the PETM and K/Pg boundary are now consistent with the intercalibration of radio-isotopic and astronomical dating methods. Previous discrepancies lie in the uncertainties of orbital solutions beyond 50 Ma and problems in the determination of the absolute age of ash -17 in the early Eocene with respect to cyclostratigraphy (Hilgen et al., 2010; Storey et al., 2007; Westerhold et al., 2009). The new accurate stratigraphy is a key to explore why and how Earth's climate shifted from greenhouse to icehouse state throughout the Paleogene in unprecedented detail. Comparison of terrestrial and deep-sea calibrations of the GPTS suggests that ages and durations of Chrons C22 and C23 need to be studied in more detail to solve current discrepancies in the future. The presently observed differences in Chrons C22 and C23 stem from uncertainties in the exact width of the stacked deep-sea anomaly profile of Cande and Kent (1992), the lack of high-quality magnetostratigraphy from deep-sea records, and uncertainties in position as well as in age of some ash layers in the terrestrial Green River Formation. Importantly the comparison between bulk carbonate carbon isotope data and orbital models for Earth's eccentricity reveals inaccuracy in the planetary ephemeris solutions and limits direct astronomical calibration using the short eccentricity cycle to 48 Ma.

Autor
Gelöscht: in unprecedented detail

Autor
Gelöscht: a

Autor
Gelöscht: an

Autor
Gelöscht: climate

Autor
Gelöscht: in

Autor
Gelöscht: good

Autor
Gelöscht:

Autor
Gelöscht: the

Acknowledgments

We thank Monika Segl and her team for stable isotope analyses at MARUM, Alexander Houben and Dyke Andreasen for stable isotope analyses at UCSC, Roy Wilkens (University of Hawaii) for introducing us into the world of core image analysis, Alex Wülbers and Walter Hale at the IODP Bremen Core Repository (BCR) for core handling, and Vera Lukies (MARUM) for assistance with XRF core scanning. This research used samples and data provided by the International Ocean Discovery Program (IODP). IODP is sponsored by the US National Science Foundation (NSF) and participating countries. Financial support for this research was provided by the Deutsche Forschungsgemeinschaft (DFG). The data reported in this paper are tabulated in the Supporting Online Material and archived at the Pangaea (www.pangaea.de) database. T.W. and U.R. designed the study, generated stable bulk isotope data for ODP Site 1263, and applied time series analysis. T. F. conducted the paleomagnetic analysis. S.B. generated the bulk isotope data for ODP Site 702, and J.Z. generated bulk isotope data for 1263. T.W., U.R., T. F., S.B. and J.Z. interpreted the data and wrote the paper.

References

Aubry, M. P.: From Chronology to Stratigraphy: Interpreting the Lower and Middle Eocene Stratigraphic Record in the Atlantic Ocean, in: Geochronology, Time Scales and Global Stratigraphic Correlation, edited by: Berggren, W. A., Kent, D. V., Aubry, M. P., and Hardenbol, J., SEPM, Spec. Publ., 213-274, 10.2110/pec.95.04.0213, 1995.

Cande, S. C., and Kent, D. V.: A New Geomagnetic Polarity Time Scale for the late Cretaceous and Cenozoic, Journal of Geophysical Research, 97, 13,917-913,951, 1992.

Cande, S. C., and Kent, D. V.: Revised calibration of the geomagnetic polarity timescale for the Late Cretaceous and Cenozoic, Journal of Geophysical Research, 100, 6093-6095, 1995.

Channell, J. E. T., Hodell, D. A., Singer, B. S., and Xuan, C.: Reconciling astrochronological and $^{40}Ar/^{39}Ar$ ages for the Matuyama-Brunhes boundary and late Matuyama Chron, Geochem. Geophys. Geosyst., 11, 21, 10.1029/2010GC003203 2010.

Charles, A. J., Condon, D. J., Harding, I. C., Pälike, H., Marshall, J. E. A., Cui, Y., Kump, L., and Croudace, I. W.: Constraints on the numerical age of the Paleocene-Eocene boundary, Geochem. Geophys. Geosyst., 12, Q0AA17, 10.1029/2010gc003426, 2011.

Clement, B. M., and Hailwood, E. A.: Magnetostratigraphy of sediments from Sites 701 and 702, in: Proc. ODP, Sci. Results, 114: College Station, TX (Ocean Drilling Program), edited by: Ciesielski, P. F., Kristoffersen, Y., and et al., 359-366, 10.2973/odp.proc.sr.114.156.1991, 1991. Place: College Station, TX, Publisher: Ocean Drilling Program, Texas A&M University

Clyde, W. C., Zonneveld, J.-P., Stamatakos, J., Gunnell, Y., and Bartels, W. S.: Magnetostratigraphy across the Wasatchian/Bridgerian NALMA Boundary (Early to Middle Eocene) in the Western Green River Basin, Wyoming, Journal of Geology, 150, 657-669, 1997.

Clyde, W. C., Sheldon, N. D., Koch, P. L., Gunnell, G. F., and Bartels, W. S.: Linking the Wasatchian/Bridgerian boundary to the Cenozoic Global Climate Optimum: new magnetostratigraphic and isotopic results from South Pass, Wyoming, Palaeogeography, Palaeoclimatology, Palaeoecology, 167, 175-199, 2001.

Clyde, W. C., Bartels, W. S., Gunnell, G. F., and Zonneveld, J.-P.: 40Ar/39Ar geochronology of the Eocene Green River Formation, Wyoming: Discussion, Geological Society of America Bulletin, 116, 251-252, 2004.

Cramer, B. S., Wright, J. D., Kent, D. V., and Aubry, M.-P.: Orbital climate forcing of $\delta^{13}C$ excursions in the late Paleocene - Eocene (chrons C24n-C25n), Paleoceanography, 18, 1097, 10.1029/2003PA000909, 2003.

Dinarès-Turell, J., Westerhold, T., Pujalte, V., Röhl, U., and Kroon, D.: Astronomical calibration of the Danian stage (Early Paleocene) revisited: Settling chronologies of sedimentary records across the Atlantic and Pacific Oceans, Earth and Planetary Science Letters, 405, 119-131, 10.1016/j.epsl.2014.08.027, 2014.

Fienga, A., Manche, H., Laskar, J., and Gastineau, M.: INPOP06: a new numerical planetary ephemeris, Astronomy & Astrophysics, 477, 315-327, 10.1051/0004-6361:20066607, 2008.

Fienga, A., Laskar, J., Morley, T., Manche, H., Kuchynka, P., Le Poncin-Lafitte, C., Budnik, F., Gastineau, M., and Somenzi, L.: INPOP08, a 4-D planetary ephemeris: from asteroid and time-scale computations to ESA Mars Express and Venus Express contributions, Astronomy & Astrophysics, 507, 1675-1686, 10.1051/0004-6361/200911755, 2009.

Fienga, A., Laskar, J., Kuchynka, P., Manche, H., Desvignes, G., Gastineau, M., Cognard, I., and Theureau, G.: The INPOP10a planetary ephemeris and its applications in fundamental physics Celestial Mechanics and Dynamical Astronomy, 111, 363-385, 10.1007/s10569-011-9377-8, 2011.

Ghil, M., Allen, M. R., Dettinger, M. D., Ide, K., Kondrashov, D., Mann, M. E., Robertson, A. W., Saunders, A., Tian, Y., Varadi, F., and Yiou, P.: Advanced Spectral Methods for Climatic Time Series, Reviews of Geophysics, 40, 1003, 10.1029/2000RG000092, 2002.

Hilgen, F. J.: Astronomical dating in the 19th century, Earth-Science Reviews, 98, 65-80, 10.1016/j.earscirev.2009.10.004, 2010.

Hilgen, F. J., Kuiper, K. F., and Lourens, L. J.: Evaluation of the astronomical time scale for the Paleocene and earliest Eocene, Earth and Planetary Science Letters, 300, 139-151, 10.1016/j.epsl.2010.09.044, 2010.

Hilgen, F. J., Abels, H. A., Kuiper, K. F., Lourens, L. J., and Wolthers, M.: Towards a stable astronomical time scale for the Paleocene: Aligning Shatsky Rise with the Zumaia – Walvis Ridge ODP Site 1262 composite, Newsletters on Stratigraphy, 48, 91-110, 10.1127/nos/2014/0054, 2015.

Hinnov, L. A., and Hilgen, F. J.: Chapter 4 - Cyclostratigraphy and Astrochronology, in: The Geologic Time Scale, edited by: Gradstein, F. M., Ogg, J. G., Schmitz, M. D., and Ogg, G. M., Elsevier, Boston, 63-83, http://dx.doi.org/10.1016/B978-0-444-59425-9.00004-4, 2012.

Hinnov, L. A.: Cyclostratigraphy and its revolutionizing applications in the earth and planetary sciences, Geological Society of America Bulletin, 125, 1703-1734, 10.1130/b30934.1, 2013.

Holbourn, A., Kuhnt, W., Clemens, S., Prell, W., and Andersen, N.: Middle to late Miocene stepwise climate cooling: Evidence from a high-resolution deep water isotope curve spanning 8 million years, Paleoceanography, 28, 2013PA002538, 10.1002/2013PA002538, 2013.

Jovane, L., Sprovieri, M., Coccioni, R., Florindo, F., Marsili, A., and Laskar, J.: Astronomical calibration of the middle Eocene Contessa Highway section (Gubbio, Italy), Earth and Planetary Science Letters, 298, 77-88, 10.1016/j.epsl.2010.07.027, 2010.

Katz, M. E., and Miller, K. G.: Early Paleogene benthic foraminiferal assemblage and stable isotopes in the Southern Ocean, in: Proc. ODP, Sci. Results, 114: College Station, TX (Ocean Drilling Program), edited by: Ciesielski, P. F., Kristoffersen, Y., and et al., 49-96, 10.2973/odp.proc.sr.114.147.1991, 1991.

Kirschvink, J. L.: The least-squares line and plane and the analysis of paleomagnetic data, Geophys. J. Roy. Astron. Soc., 62, 699-718, 10.1111/j.1365-246X.1980.tb02601.x, 1980.

Knox, R. W. O. B.: Nannoplankton zonation and the Palaeocene/Eocene boundary beds of NW Europe: an indirect correlation by means of volcanic ash layers, Journal of the Geological Society, 141, 993-999, 10.1144/gsjgs.141.6.0993, 1984.

Kuiper, K. F., Deino, A., Hilgen, F. J., Krijgsman, W., Renne, P. R., and Wijbrans, J. R.: Synchronizing Rock Clocks of Earth History, Science, 320, 500-504, 10.1126/science.1154339, 2008.

Laskar, J.: A numerical experiment on the chaotic behaviour of the Solar System, Nature, 338, 237-238, 1989.

Laskar, J., Robutel, P., Joutel, F., Gastineau, M., Correia, A., and Levrard, B.: A long-term numerical solution for the insolation quantities of the Earth, Astronomy and Astrophysics, 428, 261-285, 10.1051/0004-6361:20041335, 2004.
Laskar, J., Fienga, A., Gastineau, M., and Manche, H.: La2010: a new orbital solution for the long-term motion of the Earth, Astronomy and Astrophysics, 532, A89, 10.1051/0004-6361/201116836, 2011a.
Laskar, J., Gastineau, M., Delisle, J. B., Farrés, A., and Fienga, A.: Strong chaos induced by close encounters with Ceres and Vesta, Astronomy and Astrophysics, 532, L4, 10.1051/0004-6361/201117504, 2011b.
Littler, K., Röhl, U., Westerhold, T., and Zachos, J. C.: A high-resolution benthic stable-isotope record for the South Atlantic: Implications for orbital-scale changes in Late Paleocene–Early Eocene climate and carbon cycling, Earth and Planetary Science Letters, 401, 18-30, 10.1016/j.epsl.2014.05.054, 2014.
Lourens, L. J., Hilgen, F. J., Laskar, J., Shackleton, N. J., and Wilson, D.: The Neogene Period, in: A Geological Timescale 2004, edited by: Gradstein, F., Ogg, J., and Smith, A., 409-440, 10.1017/CBO9780511536045.022, 2004, Cambridge University Press, UK
Lurcock, P. C., and Wilson, G. S.: PuffinPlot: A versatile, user-friendly program for paleomagnetic analysis, Geochemistry, Geophysics, Geosystems, 13, Q06Z45, 10.1029/2012GC004098, 2012.
Ma, W., Tian, J., Li, Q., and Wang, P.: Simulation of long eccentricity (400-kyr) cycle in ocean carbon reservoir during Miocene Climate Optimum: Weathering and nutrient response to orbital change, Geophysical Research Letters, 38, L10701, 10.1029/2011GL047680, 2011.
Machlus, M., Hemming, S. R., Olsen, P. E., and Christie-Blick, N.: Eocene calibration of geomagnetic polarity time scale reevaluated: Evidence from the Green River Formation of Wyoming, Geology, 32, 137-140, 10.1130/G20091.1, 2004.
Machlus, M. L., Olsen, P. E., Christie-Blick, N., and Hemming, S. R.: Spectral analysis of the lower Eocene Wilkins Peak Member, Green River Formation, Wyoming: Support for Milankovitch cyclicity, Earth and Planetary Science Letters, 268, 64-75, 2008.
Machlus, M. L., Ramezani, J., Bowring, S. A., Hemming, S. R., Tsukui, K., and Clyde, W. C.: A strategy for cross-calibrating U–Pb chronology and astrochronology of sedimentary sequences: An example from the Green River Formation, Wyoming, USA, Earth and Planetary Science Letters, 413, 70-78, http://dx.doi.org/10.1016/j.epsl.2014.12.009, 2015.
Mann, M. E., and Lees, J. M.: Robust estimation of background noise and signal detection in climatic time series, Climatic Change, 33, 409-445, 10.1007/BF00142586, 1996.
Ogg, J. G., and Bardot, L.: Aptian through Eocene magnetostratigraphic correlation of the Blake Nose Transect (Leg 171B), Florida Continental Margin, in: Proc. ODP, Sci. Results, 171B: College Station, TX (Ocean Drilling Program), edited by: Kroon, D., Norris, R. D., and Klaus, A., 1-58, 10.2973/odp.proc.sr.171b.104.2001, 2001. Place: College Station, TX, Publisher: Ocean Drilling Program, Texas A&M University
Ogg, J. G., and Smith, A. G.: The geomagnetic polarity time scale, in: A Geological Timescale 2004, edited by: Gradstein, F., Ogg, J., and Smith, A., Cambridge University Press, UK, 63-86, 2004
Ogg, J. G.: Chapter 5 - Geomagnetic Polarity Time Scale, in: The Geologic Time Scale, edited by: Gradstein, F. M., Ogg, J. G., Schmitz, M. D., and Ogg, G. M., Elsevier, Boston, 85-113, http://dx.doi.org/10.1016/B978-0-444-59425-9.00005-6, 2012.
Pälike, H., Laskar, J., and Shackleton, N. J.: Geologic constraints on the chaotic diffusion of the solar system, Geology, 32, 929-932, 10.1130/G20750.1, 2004.
Pälike, H., Norris, R. D., Herrle, J. O., Wilson, P. A., Coxall, H. K., Lear, C. H., Shackleton, N. J., Tripati, A. K., and Wade, B. S.: The Heartbeat of the Oligocene Climate System, Science, 314, 1894-1898, 10.1126/science.1133822, 2006.
Pälike, H., and Hilgen, F.: Rock clock synchronization, Nature Geosci, 1, 282-282, 10.1038/ngeo197, 2008.
Pea, L.: Eocene-Oligocene paleoceanography of the subantarctic South Atlantic: Calcareous Nannofossil reconstructions of temperature, nutrient, and dissolution history, PhD., University of Parma, Parma, Italy, 205 pp., 2011.
Phillips, D., and Matchan, E. L.: Ultra-high precision $^{40}Ar/^{39}Ar$ ages for Fish Canyon Tuff and Alder Creek Rhyolite sanidine: New dating standards required?, Geochimica et Cosmochimica Acta, 121, 229-239, http://dx.doi.org/10.1016/j.gca.2013.07.003, 2013.
Renne, P. R., Swisher, C. C., Deino, A. L., Karner, D. B., Owens, T. L., and DePaolo, D. J.: Intercalibration of standards, absolute ages and uncertainties in $^{40}Ar/^{39}Ar$ dating, Chemical Geology, 145, 117-152, 1998.

Renne, P. R., Mundil, R., Balco, G., Min, K., and Ludwig, K. R.: Joint determination of ^{40}K decay constants and $^{40}Ar^{*}/^{40}K$ for the Fish Canyon sanidine standard, and improved accuracy for $^{40}Ar/^{39}Ar$ geochronology, Geochimica et Cosmochimica Acta, 74, 5349-5367, 10.1016/j.gca.2010.06.017, 2010.
Renne, P. R., Deino, A. L., Hilgen, F. J., Kuiper, K. F., Mark, D. F., Mitchell, W. S., Morgan, L. E., Mundil, R., and Smit, J.: Time Scales of Critical Events Around the Cretaceous-Paleogene Boundary, Science, 339, 684-687, 10.1126/science.1230492, 2013.
Rivera, T. A., Storey, M., Zeeden, C., Hilgen, F. J., and Kuiper, K.: A refined astronomically calibrated $^{40}Ar/^{39}Ar$ age for Fish Canyon sanidine, Earth and Planetary Science Letters, 311, 420-426, 10.1016/j.epsl.2011.09.017, 2011.
Saltzman, M. R., and Thomas, E.: Chapter 11 - Carbon Isotope Stratigraphy, in: The Geologic Time Scale, edited by: Gradstein, F. M., Ogg, J. G., Schmitz, M. D., and Ogg, G. M., Elsevier, Boston, 207-232, 10.1016/B978-0-444-59425-9.00011-1, 2012.
Sexton, P. F., Norris, R. D., Wilson, P. A., Pälike, H., Westerhold, T., Röhl, U., Bolton, C. T., and Gibbs, S.: Eocene global warming events driven by ventilation of oceanic dissolved organic carbon, Nature, 471, 349-352, 10.1038/nature09826, 2011.
Shipboard Scientific Party: Site 702, in: Proc. ODP, Init. Repts., 114: College Station, TX (Ocean Drilling Program), edited by: Ciesielski, P. F., Kristoffersen, Y., and et al., 10.2973/odp.proc.ir.114.109.1988, 1988, Place: College Station, TX, Publisher: Ocean Drilling Program, Texas A&M University
Shipboard Scientific Party: Site 1263, in: Proc. ODP, Init. Repts., 208: College Station, TX (Ocean Drilling Program), edited by: Zachos, J. C., Kroon, D., Blum, P., and et al., 1-87, 10.2973/odp.proc.ir.208.104.2004, 2004, Place: College Station, TX, Publisher: Ocean Drilling Program, Texas A&M University
Smith, E. M., Carroll, A. R., and Mueller, E. R.: Elevated weathering rates in the Rocky Mountains during the Early Eocene Climatic Optimum, Nature Geosci, 1, 370-374, 10.1038/ngeo205, 2008a.
Smith, M. E., Singer, B., and Carroll, A.: 40Ar/39Ar geochronology of the Eocene Green River Formation, Wyoming, GSA Bulletin, 115, 549-565, 10.1130/0016-7606(2003)115, 2003.
Smith, M. E., Singer, B. S., and Carroll, A. R.: Reply, Geological Society of America Bulletin, 116, 253-256, 2004.
Smith, M. E., Singer, B., Carroll, A., and Fournelle, J. H.: High-resolution calibration of Eocene strata: 40Ar/39Ar geochronology of biotite in the Green River Formation, Geology, 32, 393-396, 10.1130/G22265.1, 2006.
Smith, M. E., Carroll, A. R., and Singer, B. S.: Synoptic reconstruction of a major ancient lake system: Eocene Green River Formation, western United States, Geological Society of America Bulletin, 120, 54-84, 2008b.
Smith, M. E., Chamberlain, K. R., Singer, B. S., and Carroll, A. R.: Eocene clocks agree: Coeval 40Ar/39Ar, U-Pb, and astronomical ages from the Green River Formation, Geology, 38, 527-530, 10.1130/g30630.1, 2010.
Storey, M., Duncan, R. A., and Swisher, C. C., III: Paleocene-Eocene Thermal Maximum and the Opening of the Northeast Atlantic, Science, 316, 587-589, 10.1126/science.1135274, 2007.
Suganuma, Y., and Ogg, J. G.: Campanian through Eocene magnetostratigraphy of Sites 1257–1261, ODP Leg 207, Demerara Rise (western equatorial Atlantic), in: Proc. ODP, Sci. Results, 207: College Station, TX (Ocean Drilling Program), edited by: Mosher, D. C., Erbacher, J., and Malone, M. J., 1-48, 10.2973/odp.proc.sr.207.102.2006, 2006, Place: College Station, TX, Publisher: Ocean Drilling Program, Texas A&M University
Tsukui, K., and Clyde, W. C.: Fine-tuning the calibration of the early to middle Eocene geomagnetic polarity time scale: Paleomagnetism of radioisotopically dated tuffs from Laramide foreland basins, Geological Society of America Bulletin, 124, 870-885, 10.1130/b30545.1, 2012.
Vandenberghe, N., Hilgen, F. J., Speijer, R. P., Ogg, J. G., Gradstein, F. M., Hammer, O., Hollis, C. J., and Hooker, J. J.: Chapter 28 - The Paleogene Period, in: The Geologic Time Scale, edited by: Gradstein, F. M., Ogg, J. G., Schmitz, M. D., and Ogg, G. M., Elsevier, Boston, 855-921, http://dx.doi.org/10.1016/B978-0-444-59425-9.00028-7, 2012.
Westerhold, T., Röhl, U., Laskar, J., Bowles, J., Raffi, I., Lourens, L. J., and Zachos, J. C.: On the duration of magnetochrons C24r and C25n and the timing of early Eocene global warming events: Implications from the Ocean Drilling Program Leg 208 Walvis Ridge depth transect, Paleoceanography, 22, PA2201, 10.1029/2006PA001322, 2007.

Westerhold, T., Röhl, U., Raffi, I., Fornaciari, E., Monechi, S., Reale, V., Bowles, J., and Evans, H. F.: Astronomical calibration of the Paleocene time, Palaeogeography, Palaeoclimatology, Palaeoecology, 257, 377-403, 10.1016/j.palaeo.2007.09.016, 2008.

Westerhold, T., and Röhl, U.: High resolution cyclostratigraphy of the early Eocene - new insights into the origin of the Cenozoic cooling trend, Clim Past, 5, 309-327, 10.5194/cp-5-309-2009, 2009.

Westerhold, T., Röhl, U., McCarren, H. K., and Zachos, J. C.: Latest on the absolute age of the Paleocene-Eocene Thermal Maximum (PETM): New insights from exact stratigraphic position of key ash layers+19 and-17, Earth and Planetary Science Letters, 287, 412-419, 10.1016/j.epsl.2009.08.027, 2009.

Westerhold, T., Röhl, U., and Laskar, J.: Time scale controversy: Accurate orbital calibration of the early Paleogene, Geochem. Geophys. Geosyst., 13, Q06015, 10.1029/2012gc004096, 2012.

Westerhold, T., and Röhl, U.: Orbital pacing of Eocene climate during the Middle Eocene Climate Optimum and the Chron C19r event: Missing link found in the tropical western Atlantic, Geochemistry, Geophysics, Geosystems, 14, 4811-4825, 10.1002/ggge.20293, 2013.

Westerhold, T., Röhl, U., Pälike, H., Wilkens, R., Wilson, P. A., and Acton, G.: Orbitally tuned timescale and astronomical forcing in the middle Eocene to early Oligocene, Clim. Past, 10, 955-973, 10.5194/cp-10-955-2014, 2014.

Wotzlaw, J.-F., Bindeman, I. N., Schaltegger, U., Brooks, C. K., and Naslund, H. R.: High-resolution insights into episodes of crystallization, hydrothermal alteration and remelting in the Skaergaard intrusive complex, Earth and Planetary Science Letters, 355–356, 199-212, 10.1016/j.epsl.2012.08.043, 2012.

Wotzlaw, J.-F., Schaltegger, U., Frick, D. A., Dungan, M. A., Gerdes, A., and Günther, D.: Tracking the evolution of large-volume silicic magma reservoirs from assembly to supereruption, Geology, 41, 867-870, 10.1130/g34366.1, 2013.

Wotzlaw, J.-F., Hüsing, S. K., Hilgen, F. J., and Schaltegger, U.: High-precision zircon U–Pb geochronology of astronomically dated volcanic ash beds from the Mediterranean Miocene, Earth and Planetary Science Letters, 407, 19-34, http://dx.doi.org/10.1016/j.epsl.2014.09.025, 2014.

Zachos, J., Pagani, M., Sloan, L., Thomas, E., and Billups, K.: Trends, Rhythms, and Aberrations in Global Climate 65 Ma to Present, Science, 292, 686-693, 10.1126/science.1059412, 2001.

Zachos, J. C., McCarren, H., Murphy, B., Röhl, U., and Westerhold, T.: Tempo and scale of late Paleocene and early Eocene carbon isotope cycles: Implications for the origin of hyperthermals, Earth and Planetary Science Letters, 299, 242-249, 10.1016/j.epsl.2010.09.004, 2010.

Zeeden, C., Rivera, T. A., and Storey, M.: An astronomical age for the Bishop Tuff and concordance with radioisotopic dates, Geophysical Research Letters, 41, 2014GL059899, 10.1002/2014GL059899, 2014.

Table 1. Comparison of absolute magnetochron boundary ages in million years.

Magneto-chron	Standard GPTS			Astronomically calibrated			Astronomically calibrated – this study*		
	CK95	GPTS 2004	GPTS 2012	PEAT Sites#	Contessa Highway	ODP 1260 tuned	ODP 1258 option2	ODP 1263 tuned	ODP 702B tuned
C18n.2n (o)	40.130	39.464	40.145	**40.076 ±5**	41.120				
C19n (y)	41.257	40.439	41.154	*41.075 ±7*	41.250	**41.061 ±9**		41.030 ±13	
C19n (o)	41.521	40.671	41.390	*41.306 ±5*	41.510	**41.261 ±4**		41.180 ±11	
C20n (y)	42.536	41.590	42.301	*42.188 ±15*	42.540	**42.151 ±7**		42.107 ±13	42.124 ±4
C20n (o)	43.789	42.774	43.432		43.790	**43.449 ±18**		43.517 ±11	43.426 ±3
C21n (y)	46.264	45.346	45.724		46.310			**46.151 ±9**	46.080 ±3
C21n (o)	47.906	47.235	47.349				47.723 ±118	**47.575 ±18**	
C22n (y)	49.037	48.599	48.566				**48.954 ±16**		

* tuned to the orbital solution La2011 (Laskar et al., 2011b)

\# combined ages based on Pacific Equatorial Age Transect Sites 1218, U1333 and U1334 (Westerhold et al., 2014)

Note: **bold ages** are the best estimates to be used for developing a future reference time scale for polarity chrons

Autor
Formatierte Tabelle

Autor
Gelöscht: astronomically

Autor
Gelöscht: astronomically

Autor
Gelöscht: making

Table 2. Comparison of magnetochron boundary durations in million years.

Magneto-chron	**Standard GPTS**			**Astronomically calibrated**			**Astronomically calibrated – this study***		
	CK95	GPTS 2004	GPTS 2012	PEAT Sites#	Contessa Highway	ODP 1260 tuned	ODP 1258 option2	ODP 1263 tuned	ODP 702B tuned
C18n.2r	1.127	0.975	1.009	0.999 ±12					
C19n	0.264	0.232	0.236	*0.231 ±12*	0.260	0.200 ±7		0.150 ±24	
C19r	1.015	0.919	0.911	*0.882 ±20*	1.030	0.891 ±6		0.927 ±24	
C20n	1.253	1.184	1.131		1.250	1.297 ±13		1.410 ±24	1.302 ±7
C20r	2.475	2.572	2.292		2.520			2.634 ±20	2.654 ±6
C21n	1.642	1.889	1.625					1.424 ±27	
C21r	1.131	1.364	1.214				1.231 ±134		

* tuned to the orbital solution La2011 (Laskar et al., 2011b)

\# combined ages based on Pacific Equatorial Age Transect Sites 1218, U1333 and U1334 (Westerhold et al., 2014)

Autor
Formatierte Tabelle

Autor
Gelöscht: astronomically

Autor
Gelöscht: astronomically

Table 3. Astronomically calibrated ages of key events in the Eocene and Paleocene.

Event	Age (Ma)	Type	Source
EOT	33.89	Onset large scale glaciation of Antarctica	Westerhold et al. 2014
peak-MECO CIE	40.05	Hyperthermal	Westerhold & Röhl 2013
C19r	41.51	Hyperthermal	Westerhold & Röhl 2013
X/K (ETM-3)	52.83	Hyperthermal	Westerhold et al. 2012 Opt2
ELMO (ETM-2)	54.05	Hyperthermal	Westerhold et al. 2007 Opt2
PETM (ETM-1)	55.93	Hyperthermal	Westerhold et al. 2008 Opt2
peak-PCIM event	58.10	Shift in Pacific & Atlantic benthic carbon isotopes	Westerhold et al. 2008 Opt2
ELPE (MPBE)	59.27	Biotic turnover	Westerhold et al. 2008 Opt2
LDE (Chron 27n)	62.18	Hyperthermal	Dinarès-Turell et al. 2014
Dan C2	65.82 - 65.65	Hyperthermal	Dinarès-Turell et al. 2014
K/Pg boundary	66.022 ± 0.04	Impact	Dinarès-Turell et al. 2014

Note: Ages for the events from ELPE to X have been adjusted to La2011

Autor
Gelöscht: 02

Figure Legends

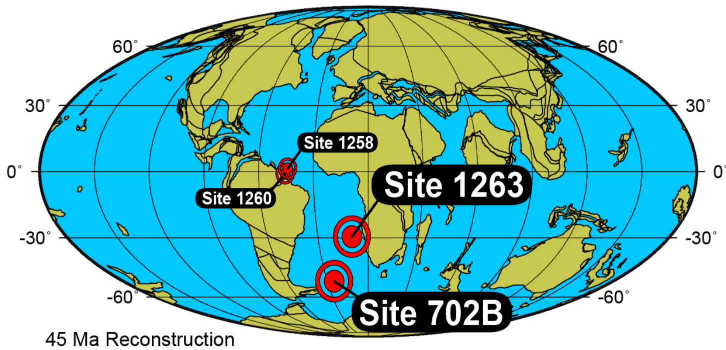

Figure 1. Location map for ODP Hole 702B and Site 1263 on a 45 Ma paleogeographic reconstruction in Mollweide projection (from http://www.odsn.de); also given location of ODP Sites 1258 and 1260.

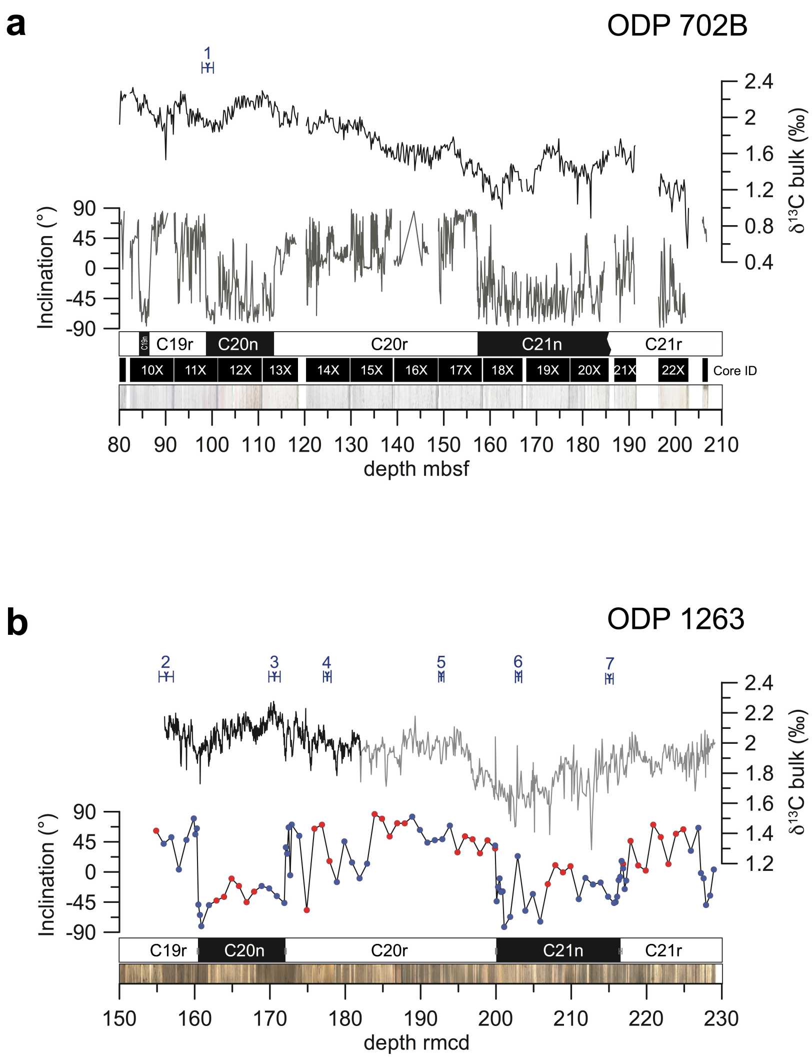

Figure 2. Overview of data from ODP Hole 702B and Site 1263 generated during this study. **a**. Bulk stable carbon (black) data generated by this study, inclination data (gray, (Clement and Hailwood, 1991)), magnetostratigraphic interpretation, core ID and core images vs. depth. **b**. ODP Site 1263 data generated by this study vs. revised composite depth: bulk stable carbon isotope data (black Bremen lab, gray Santa Cruz lab), inclination data (red dots 1263A, blue dots 1263B), magnetostratigraphic interpretation and core images. Numbers with error bars mark calcareous nannofossil events (2, 4): 1. Base *R. umbilicus* >14µm., 2. Top *Nannotetrina spp.*, 3. Top *N. fulgens*, 4. Top *C. gigas*, 5. Base *C. gigas*, 6. Base *N. fulgens*, 7. Top *D. lodoensis*.

Autor
Gelöscht: in

Autor
Gelöscht: bulk

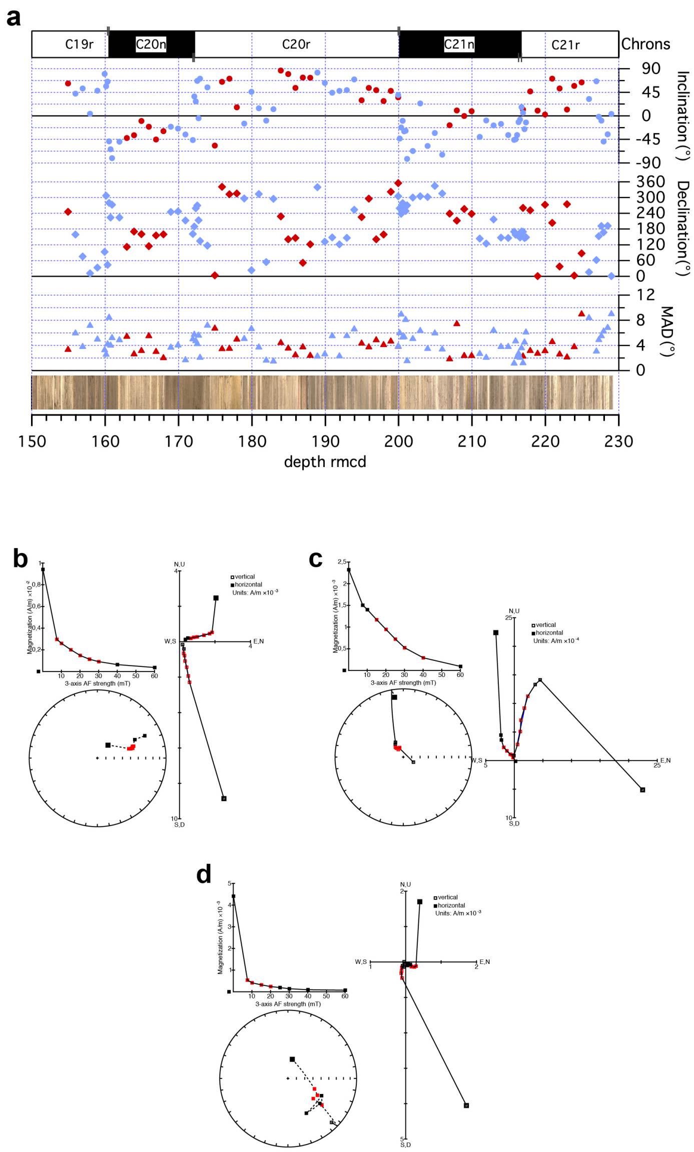

Figure 3. Magnetic property data and Zijderveld plots for ODP Site 1263. **a**. Inclination (dots), declination (diamonds) and MAD (triangles) of characteristic remanent magnetization obtained from ODP 1263. Red = 1263A, blue = 1263B. **b to d**. Showcase Zijderveld plots (z-plots) for samples from C19r 1263B10H1, 140 (b); C21n 1263B14H5, 77 (c); C21r 1263A21H6, 81 (d). Zijderveld plots were realized with PuffinPlot software (Lurcock and Wilson, 2012). For discussion see text.

Autor
Gelöscht: Characteristic

Autor
Gelöscht: Remanent

Autor
Gelöscht: Magnetization

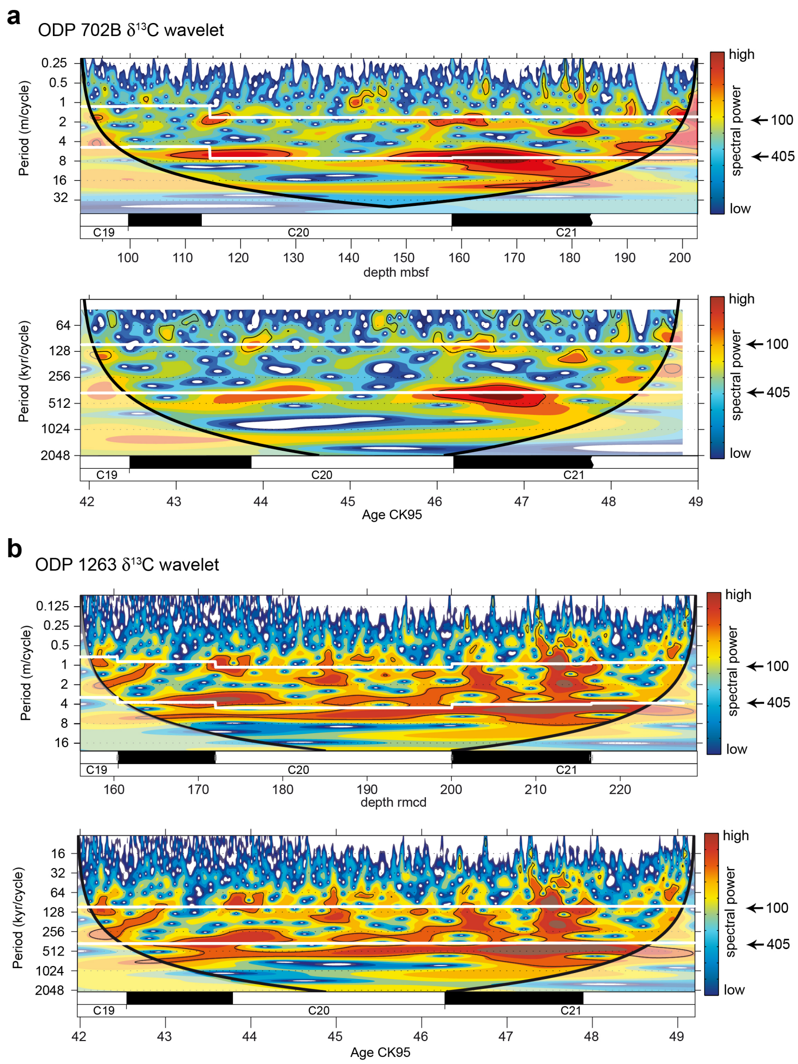

Figure 4. Evolutionary wavelet power spectra of bulk stable carbon isotope data from ODP Hole 702B (**A**) and Site 1263 (**B**) for magnetochrons C19r to C21r in the depth domain and versus age. The age model is based on magnetostratigraphy using the time scale of Cande and Kent (1995, (Cande and Kent, 1995)). The shaded contours in the evolutionary wavelet power spectra are normalized linear variances with blue representing low spectral power, and red representing high spectral power. The black contour lines enclose regions with more than 95% confidence. Shaded regions on either end indicate the cone of influence where edge effects become important. Distinct bands that run across the spectra indicate the dominance of Milankovitch frequencies. Thick white lines are the projected 100- and 405-kyr cycle path, respectively.

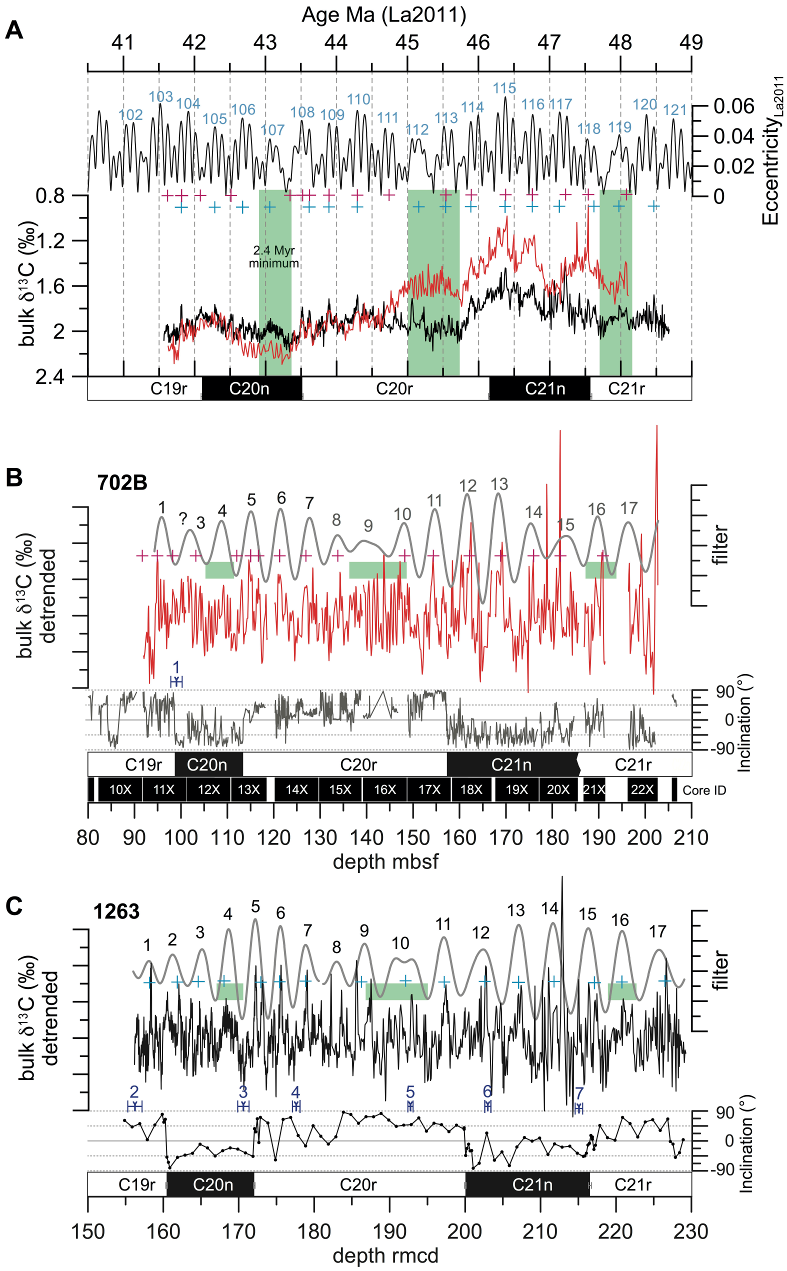

Figure 5. Middle Eocene cyclostratigraphic synthesis for ODP Sites 702 and 1263, 41–48.5 Ma. (A) Orbital eccentricity solution La2011 (Laskar et al., 2011b) and respective 405-kyr cycle number with new astronomical calibrated ages for magnetic polarity chrons

C20n, C20r and C21n. Bulk stable isotope data from Sites 702 (red) and 1263 (black) on the new astronomically tuned age model. Green bars show the minima in the amplitude modulation related to the 2.4-Myr cycle in eccentricity. (B) and (C) ODP Site 702 and 1263 detrended bulk stable isotope data and band-pass filter of the 405-kyr related eccentricity component (Site 702: 0.16 ± 0.048 cyc/m; Site 1263: 155–180 rmcd 0.29±0.087 cyc/m, 180–230 rmcd 0.23±0.069 cyc/m), paleomagnetic inclination (Clement and Hailwood, 1991), calcareous nannofossil events (Pea, 2011; Shipboard Scientific Party, 2004), core recovery for Site 702. Black numbers indicate individual 405-kyr cycles determined by combining records from both sites. Red and blue crosses indicate tuning tie points. Calcareous nannofossil events: 1. Base *R. umbilicus* >14µm, 2. Top *Nannotetrina* spp., 3. Top *N. fulgens*, 4. Top *C. gigas*, 5. Base *C. gigas*, 6. Base *N. fulgens*, 7. Top *D. lodoensis*.

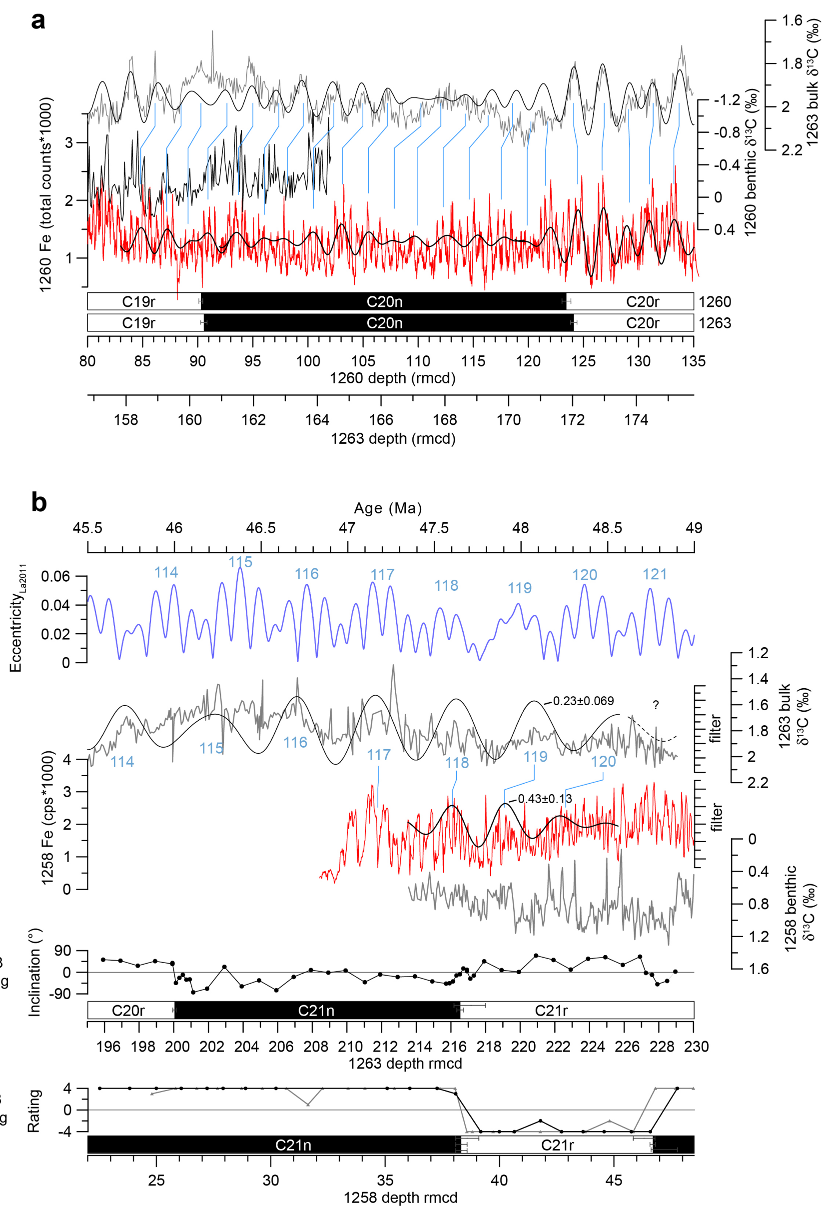

Figure 6. Connecting the 405-kyr cyclostratigraphy of ODP Sites 1258 and 1260 with Site 1263. **A**. Correlation of geochemical and paleomagnetic data from ODP Sites 1263 and 1260. Site 1260: benthic $\delta^{13}C$ in black (25), XRF core scanning Fe intensities in red

(5), magnetostratigraphy (Ogg and Bardot, 2001). Site 1263: Bulk $\delta^{13}C$ data in gray, magnetostratigraphy (both this study). For $\delta^{13}C$ and Fe data also the 100-kyr related cycle is filtered in the depth and age domain. Blue lines mark tie points between records. **B.** Tying ODP Site 1258 with the astronomically calibrated Site 1263 record at the magnetochron C21n/C21r boundary. From top to bottom: La2011 eccentricity solution; bulk $\delta^{13}C$ data and 100-kyr filter from 1263 (this study); XRF core scanning Fe intensities (Westerhold and Röhl, 2009) and benthic $\delta^{13}C$ data (Sexton et al., 2011) from 1258; inclination data and magnetostratigraphic interpretation of 1263 (this study); polarity rating scheme and magnetostratigraphic interpretation of 1258 (Suganuma and Ogg, 2006; Westerhold and Röhl, 2009). The blue numbers label the 405-kyr cycle counted back in time from today in La2011 and the respective 405-kyr cycle in 1263. The small black numbers are the filter details for 1263 $\delta^{13}C$ and 1258 Fe. The correlation of cycle 118 and 119 over the magnetochron C21n/C21r boundary using $\delta^{13}C$ data connects the cyclostratigraphy of the early Paleogene with the ATS of the Neogene and late Paleogene. This closes the mid-Eocene cyclostratigraphic gap and concludes a fully calibrated ATS for the entire Cenozoic.

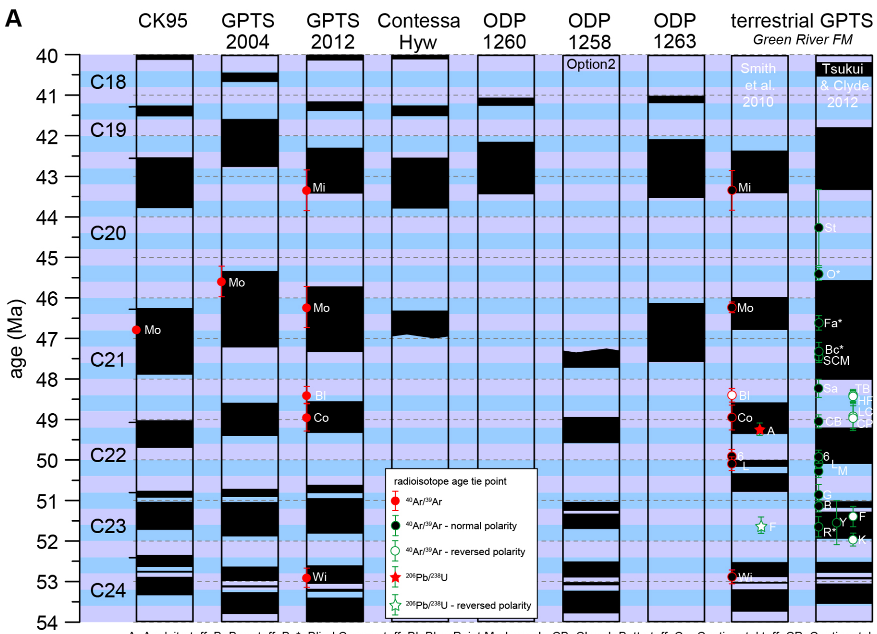

A=Analcite tuff; B=Boar tuff; Bc*=Blind Canyon tuff; Bl=Blue Point Marker ash; CB=Chruch Butte tuff; Co=Continental tuff; CP=Continental Peak tuff; Fa*=Fat tuff; F=Firehole tuff; G=Grey tuff; HF=Henry Fork tuff; K=K-spar tuff; L=Layered tuff; LC=Leavitt Creek tuff; M=Main tuff; Mi=Mission Valley ash; Mo=Montanari ash; O*=Oily tuff; R=Riffe tuff; Sa=Sage tuff; SCM=Sage Creek Mt. pumice; 6*=Sixth tuff; St=Strawberry tuff; TB=Tabernacle Butte tuff; Wi=Willwood ash; Y=Yellow tuff.

Note: all ages for terrestrial records from Smith et al. (2010) and Tsukui & Clyde (2012) are sanadine $^{40}Ar/^{39}Ar$ ages relative to 28.201 Ma for Fish Canyon sanadine (Kuiper et al. 2008); ashes markt by * are biotite ages; Analcite tuff is U/Pb age.

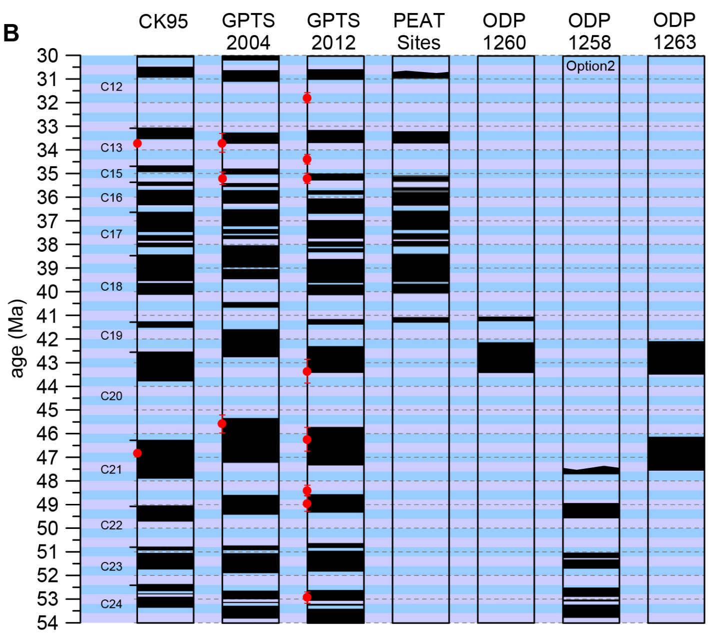

Figure 7. Geomagnetic Polarity Time Scale of CK95 (Cande and Kent, 1995), GPTS2004 (Ogg and Smith, 2004) and GPTS2012 (Ogg, 2012; Vandenberghe et al., 2012) compared to astronomical calibrations of magnetochrons from Contessa Highway (Jovane et al., 2010), PEAT sites (Westerhold et al., 2014), Site 1260 (Westerhold and Röhl, 2013), Site 1258 (Westerhold and Röhl, 2009; Westerhold et al., 2012) and 1263 (this study) from (**A**) 40-54 Ma and (**B**) 30-54 Ma. In (A) the terrestrial calibration of the GPTS from the Green River Formation (Smith et al., 2010; Tsukui & Clyde, 2012) is also shown. Small red dots with error bars mark the radio-isotopic calibration points used for CK95, GPTS2004, GPTS2012, and Smith et al. (2010); green circles show calibration points for the terrestrial sections used by Tsukui & Clyde (2012). The overview demonstrates the consistent Eocene coverage from 30-54 Ma by ODP and IODP (PEAT Sites) derived stratigraphic data, and the discrepancy to as well as in the terrestrial GPTS.

Autor
Gelöscht:

Autor
Gelöscht: Small red dots with error bars mark the radio-isotopic calibration points used for CK95, GPTS2004 and GPTS2012.

Expression of precession and short-eccentricity cycles in core images

To illustrate the possible expression of precession and short-eccentricity cycles in core images we provide two figures on Sites 702 and 1263 core data. The hierarchical expression of cyclicity or bundling of cycles is easy to recognize in the Paleocene and Maastrichtian Zumaia section (Dinarès-Turell et al., 2003; Kuiper et al., 2008; Dinarès-Turell et al., 2013; Batenburg et al., 2014; Dinarès-Turell et al., 2014). Figure S4a displays the 166 to 180 rmcd interval at Site 1263 including a 2.4 Myr minimum at approximately 168 rmcd to a more pronounced short eccentricity cyclicity below. The figure shows the individual images from two holes, 1263A and 1263B, as well as the combined (spliced) image. Slight color differences between Holes 1263A and 1263B image are related to aperture setting changes during the shipboard image acquisition. These color differences between the two holes are artifacts that cannot easily be corrected for. There is no clear expression of precession although slight changes in color may occur on decimeter level. The short eccentricity cycles appear a bit darker at $\delta^{13}C$ minima corresponding to eccentricity maxima, similar to the observations of Lourens et al. (2005) for the early Eocene. Core images of Hole 702B (Fig. S4b) are bright white with no apparent expressions of precession or short eccentricity cycles. The figure shows Cores 702B-12X and 702B-13X, time equivalents to the 1263 images of Fig. S4a. In general, core-box images taken during ODP times (“table layout images”) suffer from severe unequal lighting. Because of this most cores are darker in the upper right corner (see 702B-12X in Fig. S4b). Both ODP cores do not show the clear cycle bundling as in some outcrops on land (Zumaia) that can be utilized for astronomical tuning.

Phase relationship between bulk carbon isotopes and eccentricity

For the astronomical tuning of the bulk $\delta^{13}C$ data from 702B and 1263 lighter (more negative) $\delta^{13}C$ peaks are correlated to La2011 eccentricity maxima. The rationale for picking this phase relationship is based on several high profile studies, including modeling of carbon cycle and Earth’s orbit interaction (Zachos et al., 2001a; Cramer et al., 2003; Billups et al., 2004; Lourens et al., 2005; Pälike et al., 2006a; Pälike et al., 2006b; Holbourn et al., 2007; Tian et al., 2008; Russon et al., 2010; Zachos et al., 2010; Lunt et al., 2011; Ma et al., 2011; Sexton et al., 2011; Westerhold et al., 2011; Proistosescu et al., 2012; Holbourn et al., 2013; Kirtland Turner et al., 2014; Littler et al., 2014) dealing with the phase relation of $\delta^{13}C$ and the 405-kyr orbital eccentricity cycle. All these studies show that the Pliocene to Cenozoic $\delta^{13}C$ values in benthic and bulk deep sea carbonate reveal augmented 405-kyr cycles with minima in $\delta^{13}C$ (lighter values) and %$CaCO_3$ (i.e. peaks in Fe) corresponding to eccentricity maxima. This phase relation is also observed in the records from ODP Site 1258 (Kirtland Turner et al., 2014) and 1260 (Edgar et al., 2007) as shown herein. The $\delta^{13}C$ cycles are consistent with a climate-carbon cycle feedback, as indicated by a relative lag in $\delta^{13}C$ relative to $\delta^{18}O$. The strong 405-kyr cycle in benthic and bulk $\delta^{13}C$ data as well as simulated $\delta^{13}C$ results from a resonance associated with the long residence time of carbon in the ocean (Broecker and Peng, 1982; Pälike et al., 2006a; Ma et al., 2011). Periodic changes in oceanic $\delta^{13}C$ on Milankovitch time scales are likely caused by changes in weathering induced carbon input changing the burial ratio of $CaCO_3$ to organic carbon (Cramer et al., 2003; Ma et al., 2011). An increase in weathering intensity and riverine carbon supply will increase the burial ratio of $CaCO_3$ to organic carbon leading to a decrease in $\delta^{13}C$ (minima, lighter values in bulk $\delta^{13}C$). During eccentricity maxima weathering intensity and nutrient supply is enhanced leading via the biosphere productivity feedback to lighter bulk $\delta^{13}C$ values in the stable carbon isotope records. The phase lag of $\delta^{13}C$ to eccentricity has been estimated to be in the order of 50 and 10 kyr for long and short eccentricity (Herbert, 1997; Zachos et al., 2001b; Holbourn et al., 2007; Zachos et al., 2010; Westerhold et al., 2011) in the Neogene and Paleogene. This leads to the assumption that the uncertainty in astronomical tuning presented here is in the order of less than 50 kyr. In fact the main uncertainty derives from the error in the 405-kyr eccentricity cycle in the order of 50 kyr at 56 Ma and 60 kyr at 66 Ma.

References:

Batenburg, S. J., Gale, A. S., Sprovieri, M., Hilgen, F. J., Thibault, N., Boussaha, M., and Orue-Etxebarria, X.: An astronomical time scale for the Maastrichtian based on the Zumaia and Sopelana sections (Basque country, northern Spain), Journal of the Geological Society, 10.1144/jgs2013-015, 2014.

Billups, K., Palike, H., Channell, J. E. T., Zachos, J. C., and Shackleton, N. J.: Astronomic calibration of the late Oligocene through early Miocene geomagnetic polarity time scale, Earth and Planetary Science Letters, 224, 33-44, 2004.

Broecker, W. S., and Peng, T. H.: Tracers in the Sea, edited by: University, C., Lamont Doherty Geol. Obs. Publications, New York, 689 pp., 1982.

Channell, J. E. T., Hodell, D. A., Singer, B. S., and Xuan, C.: Reconciling astrochronological and $^{40}Ar/^{39}Ar$ ages for the Matuyama-Brunhes boundary and late Matuyama Chron, Geochem. Geophys. Geosyst., 11, 21, 10.1029/2010GC003203 2010.

Charles, A. J., Condon, D. J., Harding, I. C., Pälike, H., Marshall, J. E. A., Cui, Y., Kump, L., and Croudace, I. W.: Constraints on the numerical age of the Paleocene-Eocene boundary, Geochem. Geophys. Geosyst., 12, Q0AA17, 10.1029/2010gc003426, 2011.

Cramer, B. S., Wright, J. D., Kent, D. V., and Aubry, M.-P.: Orbital climate forcing of $\delta^{13}C$ excursions in the late Paleocene - Eocene (chrons C24n-C25n), Paleoceanography, 18, 1097, 10.1029/2003PA000909, 2003.

Dinarès-Turell, J., Baceta, J. I., Pujalte, V., Orue-Etxebarria, X., Bernaola, G., and Lorito, S.: Untangling the Paleocene climatic rhythm: an astronomically calibrated Early Paleocene magnetostratigraphy and biostratigraphy at Zumaia (Basque basin, northern Spain), Earth and Planetary Science Letters, 216, 483-500, 2003.

Dinarès-Turell, J., Pujalte, V., Stoykova, K., and Elorza, J.: Detailed correlation and astronomical forcing within the Upper Maastrichtian succession in the Basque Basin, Boletín Geológico y Minero, 124, 253-282, 2013.

Dinarès-Turell, J., Westerhold, T., Pujalte, V., Röhl, U., and Kroon, D.: Astronomical calibration of the Danian stage (Early Paleocene) revisited: Settling chronologies of sedimentary records across the Atlantic and Pacific Oceans, Earth and Planetary Science Letters, 405, 119-131, 10.1016/j.epsl.2014.08.027, 2014.

Edgar, K. M., Wilson, P. A., Sexton, P. F., and Suganuma, Y.: No extreme bipolar glaciation during the main Eocene calcite compensation shift, Nature, 448, 908-911, 10.1038/nature06053, 2007.

Herbert, T. D.: A long marine history of carbon cycle modulation by orbital-climatic changes, Proc. Natl. Acad. Sci. USA, 94, 8362-8369, 1997.

Holbourn, A., Kuhnt, W., Schulz, M., Flores, J.-A., and Andersen, N.: Orbitally-paced climate evolution during the middle Miocene "Monterey" carbon-isotope excursion, Earth and Planetary Science Letters, 261, 534-550, 2007.

Holbourn, A., Kuhnt, W., Clemens, S., Prell, W., and Andersen, N.: Middle to late Miocene stepwise climate cooling: Evidence from a high-resolution deep water isotope curve spanning 8 million years, Paleoceanography, 28, 2013PA002538, 10.1002/2013PA002538, 2013.

Kirtland Turner, S., Sexton, P. F., Charles, C. D., and Norris, R. D.: Persistence of carbon release events through the peak of early Eocene global warmth, Nature Geosci, 7, 10.1038/ngeo2240, 2014.

Kuiper, K. F., Deino, A., Hilgen, F. J., Krijgsman, W., Renne, P. R., and Wijbrans, J. R.: Synchronizing Rock Clocks of Earth History, Science, 320, 500-504, 10.1126/science.1154339, 2008.
Laskar, J., Fienga, A., Gastineau, M., and Manche, H.: La2010: a new orbital solution for the long-term motion of the Earth, Astronomy and Astrophysics, 532, A89, 10.1051/0004-6361/201116836, 2011a.
Laskar, J., Gastineau, M., Delisle, J. B., Farrés, A., and Fienga, A.: Strong chaos induced by close encounters with Ceres and Vesta, Astronomy and Astrophysics, 532, L4, 10.1051/0004-6361/201117504, 2011b.
Littler, K., Röhl, U., Westerhold, T., and Zachos, J. C.: A high-resolution benthic stable-isotope record for the South Atlantic: Implications for orbital-scale changes in Late Paleocene–Early Eocene climate and carbon cycling, Earth and Planetary Science Letters, 401, 18-30, 10.1016/j.epsl.2014.05.054, 2014.
Lourens, L. J., Sluijs, A., Kroon, D., Zachos, J. C., Thomas, E., Röhl, U., Bowles, J., and Raffi, I.: Astronomical pacing of late Palaeocene to early Eocene global warming events, Nature, 435, 1083-1087, 10.1038/nature03814, 2005.
Lunt, D. J., Ridgwell, A., Sluijs, A., Zachos, J., Hunter, S., and Haywood, A.: A model for orbital pacing of methane hydrate destabilization during the Palaeogene, Nature Geosci, 4, 775-778, 10.1038/ngeo1266, 2011.
Ma, W., Tian, J., Li, Q., and Wang, P.: Simulation of long eccentricity (400-kyr) cycle in ocean carbon reservoir during Miocene Climate Optimum: Weathering and nutrient response to orbital change, Geophysical Research Letters, 38, L10701, 10.1029/2011GL047680, 2011.
Pälike, H., Frazier, J., and Zachos, J. C.: Extended orbitally forced palaeoclimatic records from the equatorial Atlantic Ceara Rise, Quaternary Science Reviews, 25, 3138-3149, 2006a.
Pälike, H., Norris, R. D., Herrle, J. O., Wilson, P. A., Coxall, H. K., Lear, C. H., Shackleton, N. J., Tripati, A. K., and Wade, B. S.: The Heartbeat of the Oligocene Climate System, Science, 314, 1894-1898, 10.1126/science.1133822, 2006b.
Proistosescu, C., Huybers, P., and Maloof, A. C.: To tune or not to tune: Detecting orbital variability in Oligo-Miocene climate records, Earth and Planetary Science Letters, 325–326, 100-107, 10.1016/j.epsl.2012.01.022, 2012.
Renne, P. R., Swisher, C. C., Deino, A. L., Karner, D. B., Owens, T. L., and DePaolo, D. J.: Intercalibration of standards, absolute ages and uncertainties in $^{40}Ar/^{39}Ar$ dating, Chemical Geology, 145, 117-152, 1998.
Renne, P. R., Mundil, R., Balco, G., Min, K., and Ludwig, K. R.: Joint determination of ^{40}K decay constants and $^{40}Ar^{*}/^{40}K$ for the Fish Canyon sanidine standard, and improved accuracy for $^{40}Ar/^{39}Ar$ geochronology, Geochimica et Cosmochimica Acta, 74, 5349-5367, 10.1016/j.gca.2010.06.017, 2010.
Rivera, T. A., Storey, M., Zeeden, C., Hilgen, F. J., and Kuiper, K.: A refined astronomically calibrated $^{40}Ar/^{39}Ar$ age for Fish Canyon sanidine, Earth and Planetary Science Letters, 311, 420-426, 10.1016/j.epsl.2011.09.017, 2011.
Russon, T., Paillard, D., and Elliot, M.: Potential origins of 400–500 kyr periodicities in the ocean carbon cycle: A box model approach, Global Biogeochemical Cycles, 24, GB2013, 10.1029/2009GB003586, 2010.
Sexton, P. F., Norris, R. D., Wilson, P. A., Pälike, H., Westerhold, T., Röhl, U., Bolton, C. T., and Gibbs, S.: Eocene global warming events driven by ventilation of oceanic dissolved organic carbon, Nature, 471, 349-352, 10.1038/nature09826, 2011.
Shipboard Scientific Party: Site 1263, in: Proc. ODP, Init. Repts., 208: College Station, TX (Ocean Drilling Program), edited by: Zachos, J. C., Kroon, D., Blum, P., and et al., 1-87, 10.2973/odp.proc.ir.208.104.2004, 2004.
Tian, J., Zhao, Q., Wang, P., Li, Q., and Cheng, X.: Astronomically modulated Neogene sediment records from the South China Sea, Paleoceanography, 23, 10.1029/2007PA001552, 2008.
Westerhold, T., Röhl, U., Laskar, J., Bowles, J., Raffi, I., Lourens, L. J., and Zachos, J. C.: On the duration of magnetochrons C24r and C25n and the timing of early Eocene global warming events: Implications from the Ocean Drilling Program Leg 208 Walvis Ridge depth transect, Paleoceanography, 22, 10.1029/2006PA001322, 2007.
Westerhold, T., Röhl, U., Raffi, I., Fornaciari, E., Monechi, S., Reale, V., Bowles, J., and Evans, H. F.: Astronomical calibration of the Paleocene time, Palaeogeography, Palaeoclimatology, Palaeoecology, 257, 377-403, 10.1016/j.palaeo.2007.09.016, 2008.
Westerhold, T., and Röhl, U.: High resolution cyclostratigraphy of the early Eocene - new insights into the origin of the Cenozoic cooling trend, Clim Past, 5, 309-327, 10.5194/cp-5-309-2009, 2009.
Westerhold, T., Röhl, U., McCarren, H. K., and Zachos, J. C.: Latest on the absolute age of the Paleocene-Eocene Thermal Maximum (PETM): New insights from exact stratigraphic position of key ash layers+19 and-17, Earth and Planetary Science Letters, 287, 412-419, 10.1016/j.epsl.2009.08.027, 2009.
Westerhold, T., Röhl, U., Donner, B., McCarren, H. K., and Zachos, J. C.: A complete high-resolution Paleocene benthic stable isotope record for the central Pacific (ODP Site 1209), Paleoceanography, 26, PA2216, 10.1029/2010pa002092, 2011.
Westerhold, T., Röhl, U., and Laskar, J.: Time scale controversy: Accurate orbital calibration of the early Paleogene, Geochem. Geophys. Geosyst., 13, Q06015, 10.1029/2012gc004096, 2012.
Zachos, J., Pagani, M., Sloan, L., Thomas, E., and Billups, K.: Trends, Rhythms, and Aberrations in Global Climate 65 Ma to Present, Science, 292, 686-693, 10.1126/science.1059412, 2001a.
Zachos, J., Shackleton, N. J., Revenaugh, J. S., Pälike, H., and Flower, B. P.: Climate Response to Orbital Forcing Across the Oligocene-Miocene Boundary, Science, 292, 274-278, 10.1126/science.1058288, 2001b.
Zachos, J. C., McCarren, H., Murphy, B., Röhl, U., and Westerhold, T.: Tempo and scale of late Paleocene and early Eocene carbon isotope cycles: Implications for the origin of hyperthermals, Earth and Planetary Science Letters, 299, 242-249, 10.1016/j.epsl.2010.09.004, 2010.

Figure Legends

Figure S1. ODP Site 1263 magnetic susceptibility data (Shipboard Scientific Party, 2004) from Holes A (red), B (blue) and C (green) on the new revised composite depth. Data and core images are plotted for each hole separately. Red vertical lines are the tops and yellow vertical lines are the bases of splice sections. All magnetic susceptibility data are the instrument units raw in 10^{-5}.

Figure S2. MTM power spectra of ODP Hole 702B bulk $\delta^{13}C$ data from various intervals in the depth and age (magnetostratigraphy ages CK95) domain.

Figure S3. MTM power spectra of ODP Site 1263 bulk $\delta^{13}C$ data from various intervals in the depth and age (magnetostratigraphy ages CK95) domain.

Figure S4. Close up of ODP Site 1263 and Hole 702B to illustrate the potential expression of precession and short-eccentricity cycles in core images.

Figure S5. Comparison of sedimentation rates for Site 1263 and Hole 702B records using the tuned, the magnetostratigraphic, the 17 405-kyr cyclo- and 18 405-kyr cyclostratigraphic age model. Bulk $\delta^{13}C$ data (gray) and the magnetostratigraphy are also shown.

Figure S6. Eccentricity solutions La2010a-d (Laskar et al., 2011a) and La2011 (Laskar et al., 2011b) of the Earth (fine black line) compared to geological data to assess the positions of the 2.4 myr eccentricity cycle minima from 41 to 60 Ma. To accentuate successive minima in the eccentricity solution the amplitude modulation (AM) was extracted from the orbital solution (thick gray line). Geochemical data with a dominant eccentricity component are plotted on the stable 405-kyr cyclostratigraphic framework anchored to the ATS. Data: bulk $\delta^{13}C$ from 1258 in light blue (Kirtland Turner et al., 2014), 1262 in bright blue (Littler et al., 2014; Zachos et al., 2010) and 1263 in dark blue (this study); benthic $\delta^{13}C$ from 1258 in gray (Sexton et al., 2011); XRF core scanning iron (Fe) intensity data from 1262 in orange (Westerhold et al., 2007; Westerhold et al., 2008) and 1258 in red (Westerhold and Röhl, 2009). Also given is the position of the Paleocene-Eocene Thermal Maximum (PETM) (Westerhold et al., 2007) and ash -17 (Westerhold et al., 2009). Light blue bars mark the 2.4 myr eccentricity minima in the geological data. The comparison shows that none of the orbital solutions matches all of the minima in the geological records back to 60 Ma. La2011 and La2010d reproduce all minima up to 48 Ma. Therefore, for astronomical dating only these two solutions are robust back to 48 Ma. For older times only the stable 405-kyr eccentricity cycle should be utilized.

Figure S7. Comparison of astronomical and radio-isotopic ages for the Paleocene-Eocene Thermal Maximum (PETM) and ash -17. Gray bars mark the absolute age range for the onset of the PETM based on the age and relative distance of ash -17 with respect to the age of the Fish Canyon (FC) radiometric dating $^{40}Ar/^{39}Ar$ standard of 28.02 (Renne et al., 1998), 28.201 (Kuiper et al., 2008), 28.305 (Renne et al., 2010), 27.93 (Channell et al., 2010), 27.89 (Westerhold et al., 2012), 28.172 (Rivera et al., 2011) and 28.10 (this study) Ma. Horizontal black lines mark the three possible options of the age range for the onset of the PETM based on the astronomically calibrated Paleocene time scale (Westerhold et al., 2008). The red bar and arrow as well as light blue bar and arrow mark the astronomically calibrated absolute age for the onset of the PETM and ash -17 consistent with the 2.4 myr minima in the La2011 orbital solution (Westerhold et al., 2012). The green bar and arrow as well as the blue bar and arrow mark the age of the onset of the PETM and ash -17 consistent with the stable 405-kyr cyclostratigraphy established in this study. The black double dot with error bar shows the age of the onset of the PETM based on a high precision radio-isotopic U/Pb age of 55.728 - 55.964 Ma from bentonite layers within the PETM interval at Spitzbergen (Charles et al., 2011). The U/Pb age and the stable 405-kyr cyclostratigraphy age of ~55.9 Ma are independent from uncertainties in the 100-kyr and 2.4 myr eccentricity cycle components and therefore the most robust age for the onset of the PETM.

Figure S8. Detailed graph of bulk $\delta^{13}C$ data from 702B (red) and 1263 (black) plotted on the tuned age model. (A) Both records plotted on the same $\delta^{13}C$ axis. Benthic foraminifers' $\delta^{13}C$ data from Katz and Miller (1991). (B) Zoom of the 46.5 to 48.2 Ma interval plotted on a separate $\delta^{13}C$ axes. Black lines mark lighter $\delta^{13}C$ values at 702B at 47.23, 47.39, 47.55 and 48.08 Ma that correlate with lighter values in 1263. Note that the 47.39 and 47.55 Ma peaks at 702B are single data points and that due to the sample resolution of 20 cm at 702B in this interval transient $\delta^{13}C$ excursions could be missed.

Autor
Gelöscht: i

Autor
Gelöscht: The b

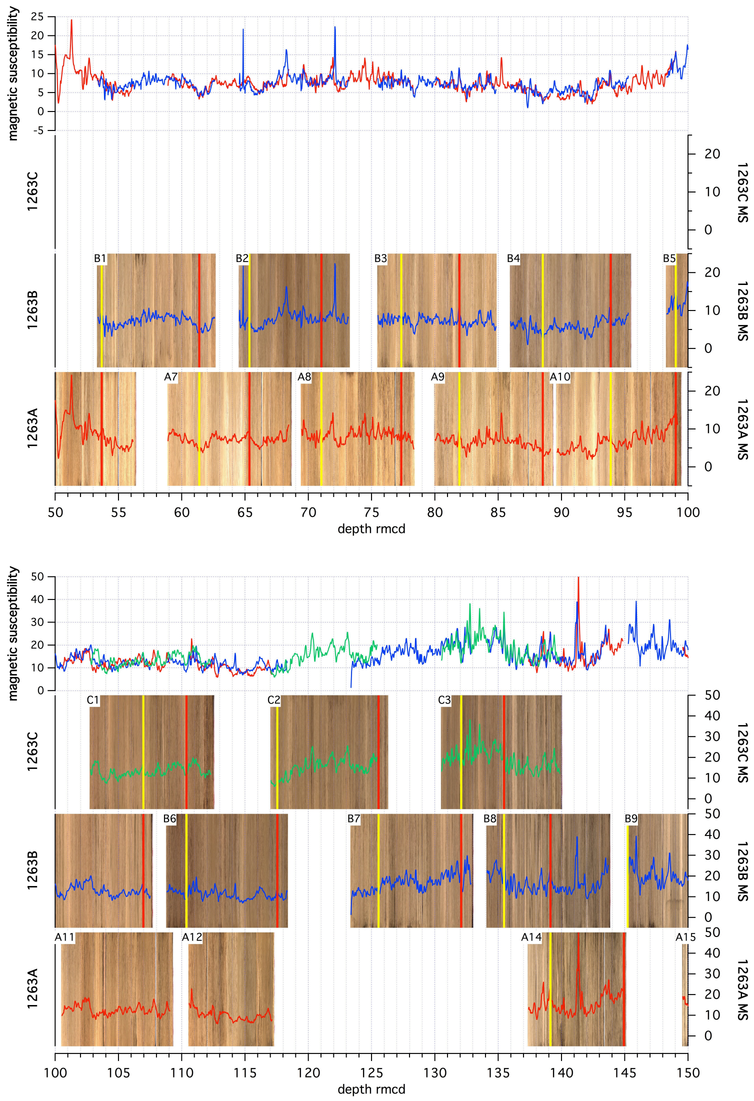
magnetic susceptibility
1263C
1263B
1263A
1263C MS
1263B MS
1263A MS
B1
B2
B3
B4
B5
A7
A8
A9
A10
C1
C2
C3
B6
B7
B8
B9
A11
A12
A14
A15
depth rmcd

Figure S1

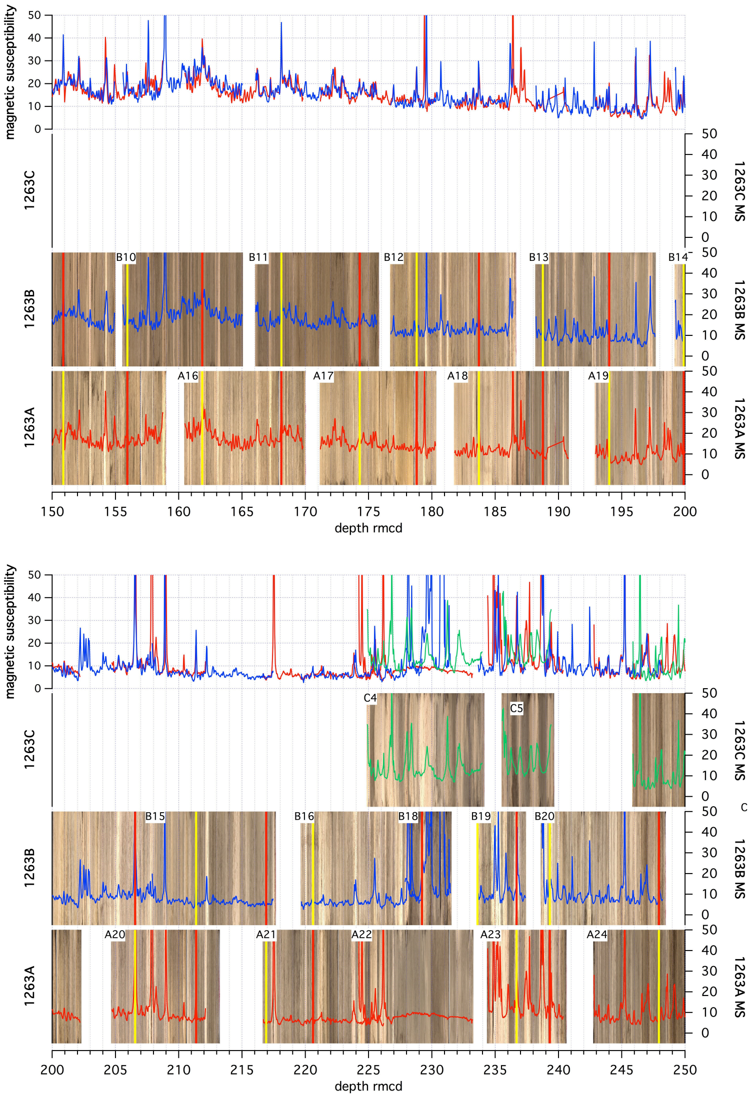

Figure S1 - continued.

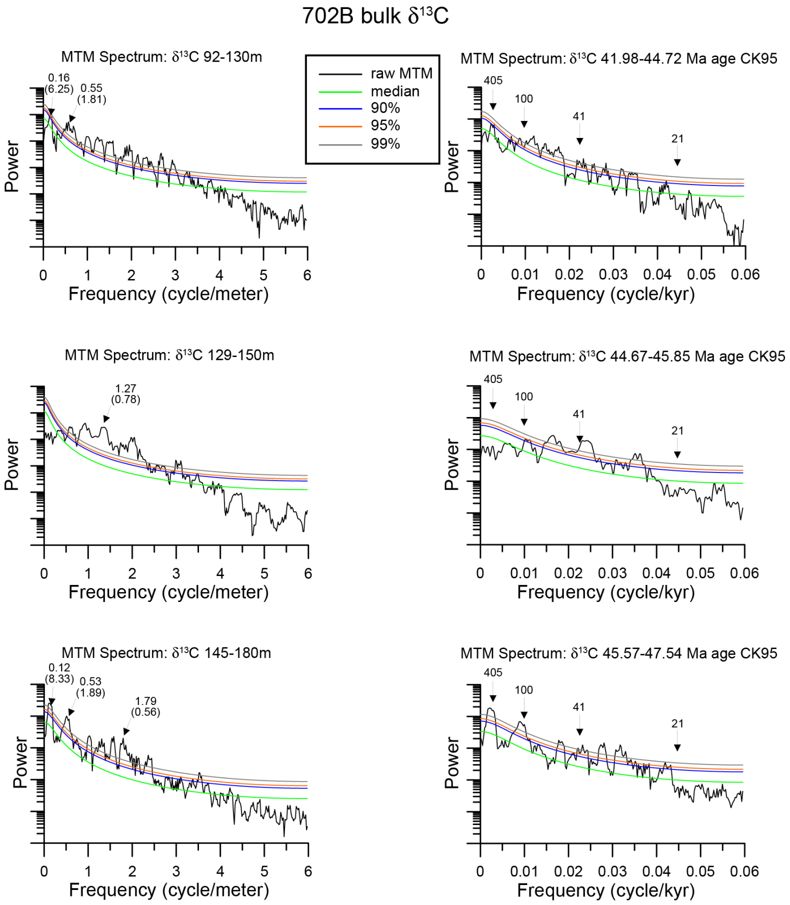
702B bulk δ13C
MTM Spectrum: δ13C 92-130m
0.16
(6.25)
0.55
(1.81)
raw MTM
median
90%
95%
99%
MTM Spectrum: δ13C 41.98-44.72 Ma age CK95
405
100
41
21
MTM Spectrum: δ13C 129-150m
1.27
(0.78)
MTM Spectrum: δ13C 44.67-45.85 Ma age CK95
MTM Spectrum: δ13C 145-180m
0.12
(8.33)
0.53
(1.89)
1.79
(0.56)
MTM Spectrum: δ13C 45.57-47.54 Ma age CK95
Power
Frequency (cycle/meter)
Frequency (cycle/kyr)

Figure S2

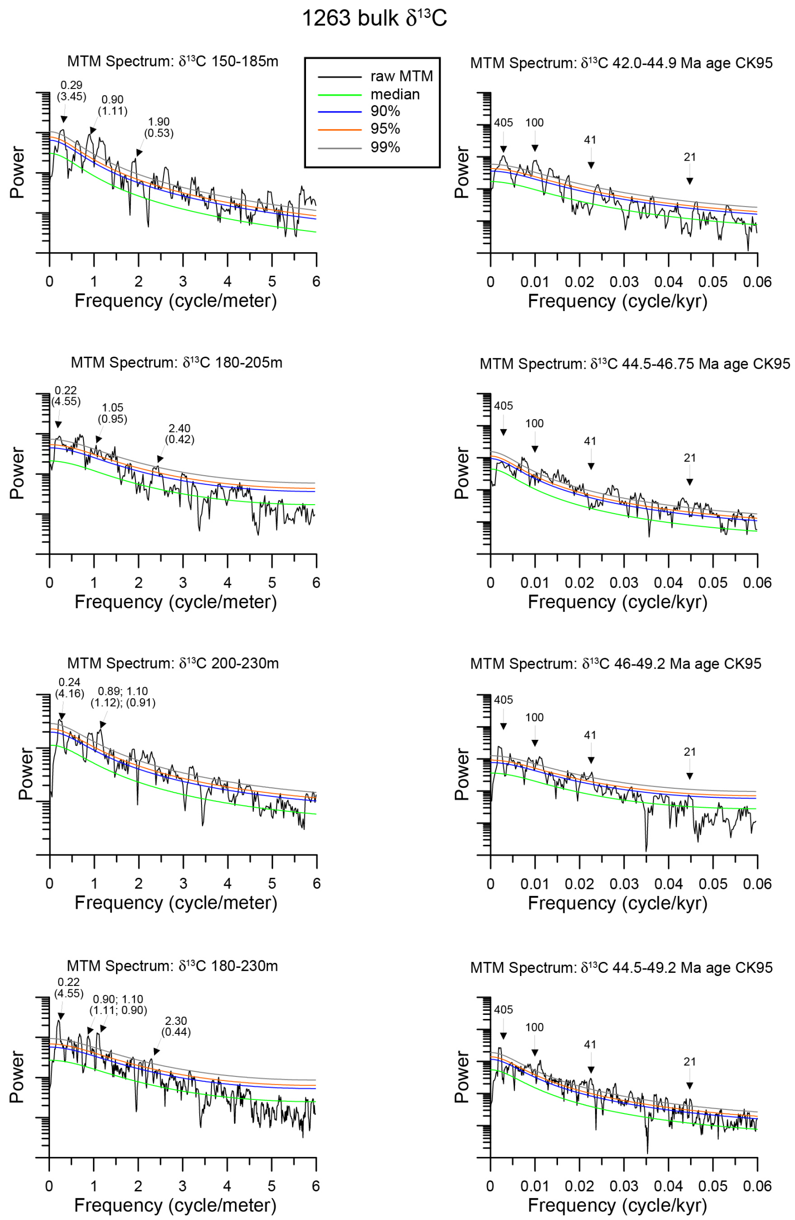

1263 bulk δ13C
MTM Spectrum: δ13C 150-185m
0.29 (3.45)
0.90 (1.11)
1.90 (0.53)
raw MTM
median
90%
95%
99%
MTM Spectrum: δ13C 42.0-44.9 Ma age CK95
405
100
41
21
MTM Spectrum: δ13C 180-205m
0.22 (4.55)
1.05 (0.95)
2.40 (0.42)
MTM Spectrum: δ13C 44.5-46.75 Ma age CK95
MTM Spectrum: δ13C 200-230m
0.24 (4.16)
0.89; 1.10 (1.12); (0.91)
MTM Spectrum: δ13C 46-49.2 Ma age CK95
MTM Spectrum: δ13C 180-230m
0.22 (4.55)
0.90; 1.10 (1.11; 0.90)
2.30 (0.44)
MTM Spectrum: δ13C 44.5-49.2 Ma age CK95
Power
Frequency (cycle/meter)
Frequency (cycle/kyr)

Figure S3

a,

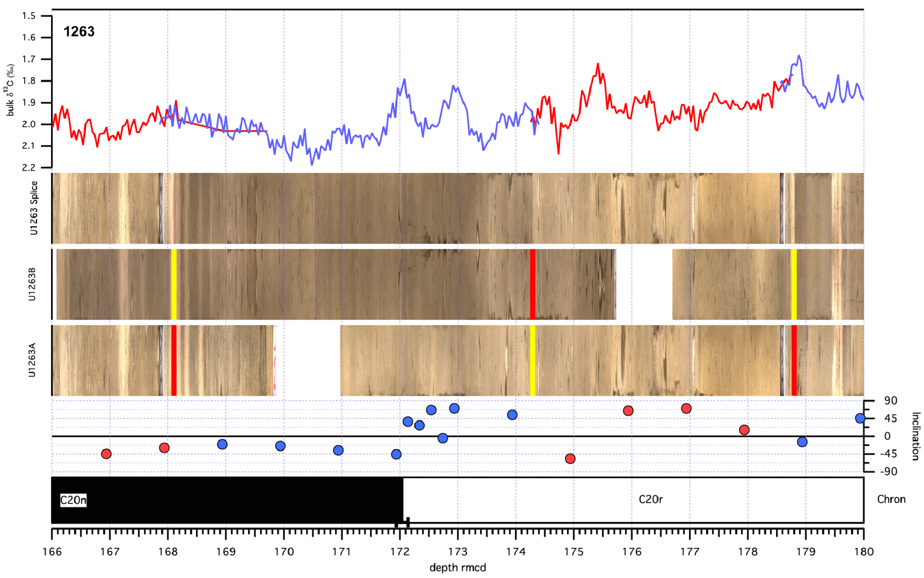

1263
bulk δ13C (‰)
U1263 Splice
U1263B
U1263A
Inclination
Chron
C20n
C20r
depth rmcd

b,

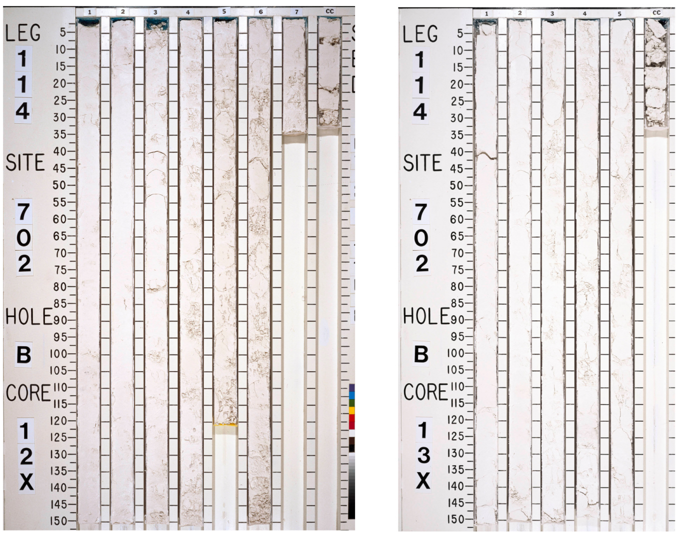

LEG 114 SITE 702 HOLE B CORE 12X
LEG 114 SITE 702 HOLE B CORE 13X

Figure S4

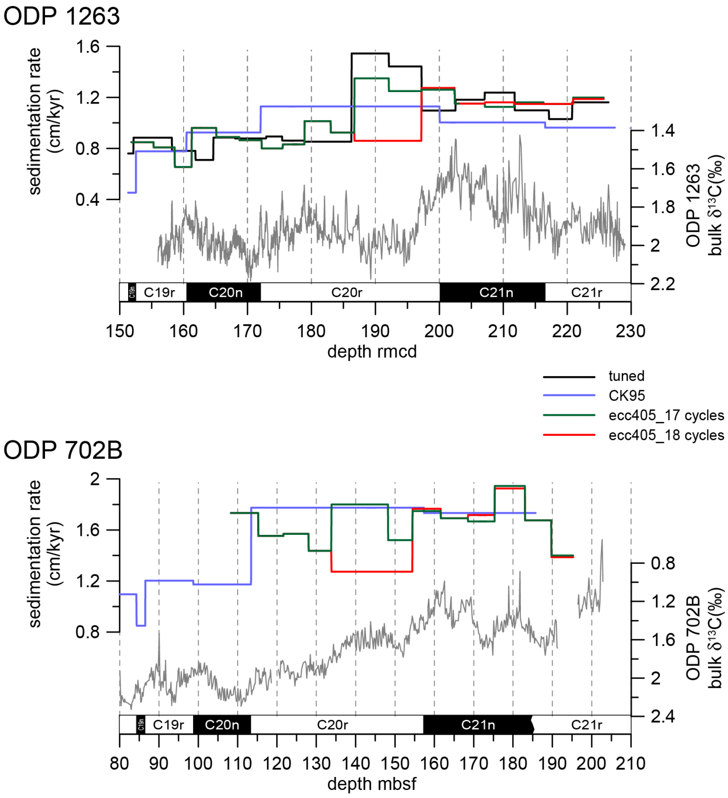

ODP 1263
sedimentation rate (cm/kyr)
ODP 1263 bulk δ13C(‰)
C19r
C20n
C20r
C21n
C21r
depth rmcd
tuned
CK95
ecc405_17 cycles
ecc405_18 cycles
ODP 702B
sedimentation rate (cm/kyr)
ODP 702B bulk δ13C(‰)
C19r
C20n
C20r
C21n
C21r
depth mbsf

Figure S5

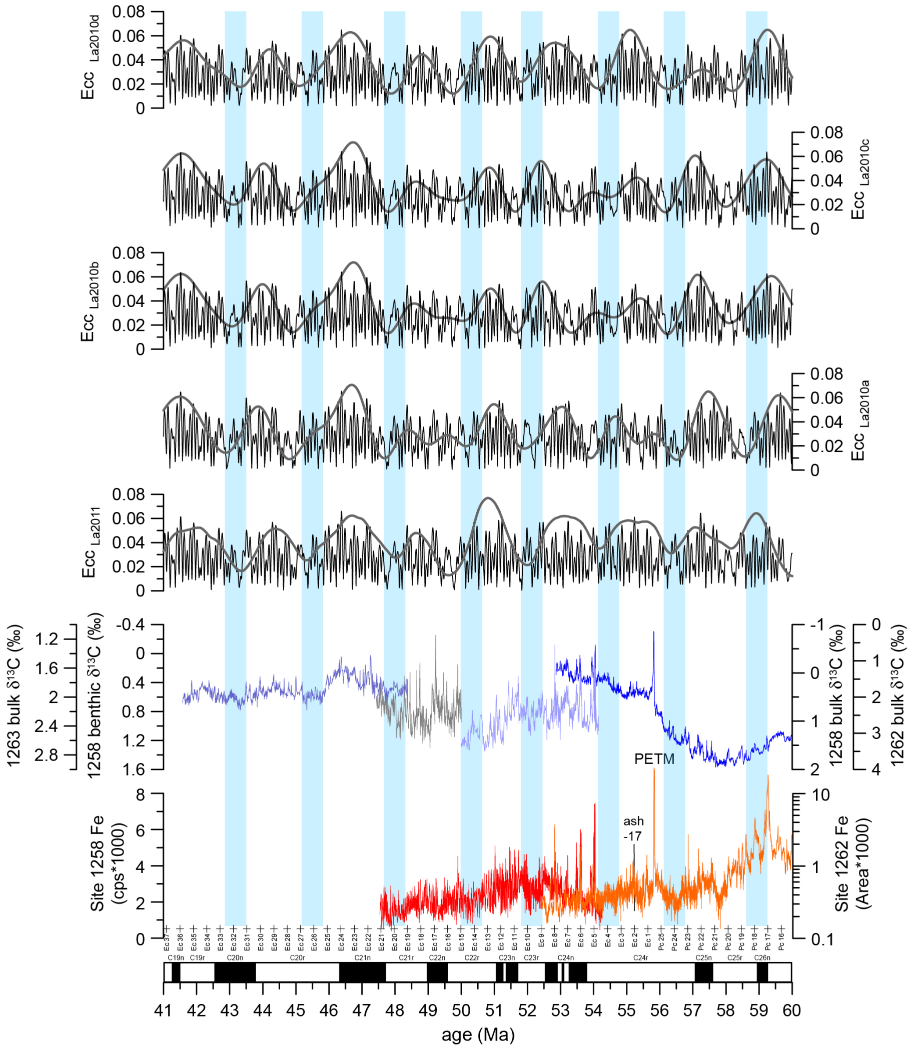

Ecc La2010d
Ecc La2010c
Ecc La2010b
Ecc La2010a
Ecc La2011
1263 bulk δ13C (‰)
1258 benthic δ13C (‰)
1258 bulk δ13C (‰)
1262 bulk δ13C (‰)
PETM
ash -17
Site 1258 Fe (cps*1000)
Site 1262 Fe (Area*1000)
age (Ma)

Figure S6

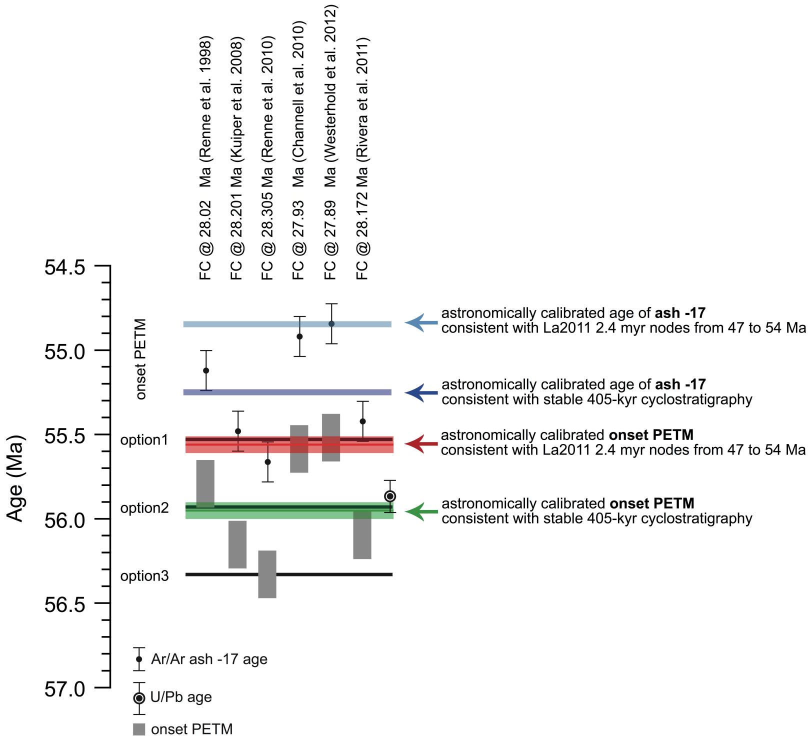
FC @ 28.02 Ma (Renne et al. 1998)
FC @ 28.201 Ma (Kuiper et al. 2008)
FC @ 28.305 Ma (Renne et al. 2010)
FC @ 27.93 Ma (Channell et al. 2010)
FC @ 27.89 Ma (Westerhold et al. 2012)
FC @ 28.172 Ma (Rivera et al. 2011)
Age (Ma)
54.5
55.0
55.5
56.0
56.5
57.0
onset PETM
option1
option2
option3
astronomically calibrated age of **ash -17**
consistent with La2011 2.4 myr nodes from 47 to 54 Ma
astronomically calibrated age of **ash -17**
consistent with stable 405-kyr cyclostratigraphy
astronomically calibrated **onset PETM**
consistent with La2011 2.4 myr nodes from 47 to 54 Ma
astronomically calibrated **onset PETM**
consistent with stable 405-kyr cyclostratigraphy
Ar/Ar ash -17 age
U/Pb age
onset PETM

Figure S7

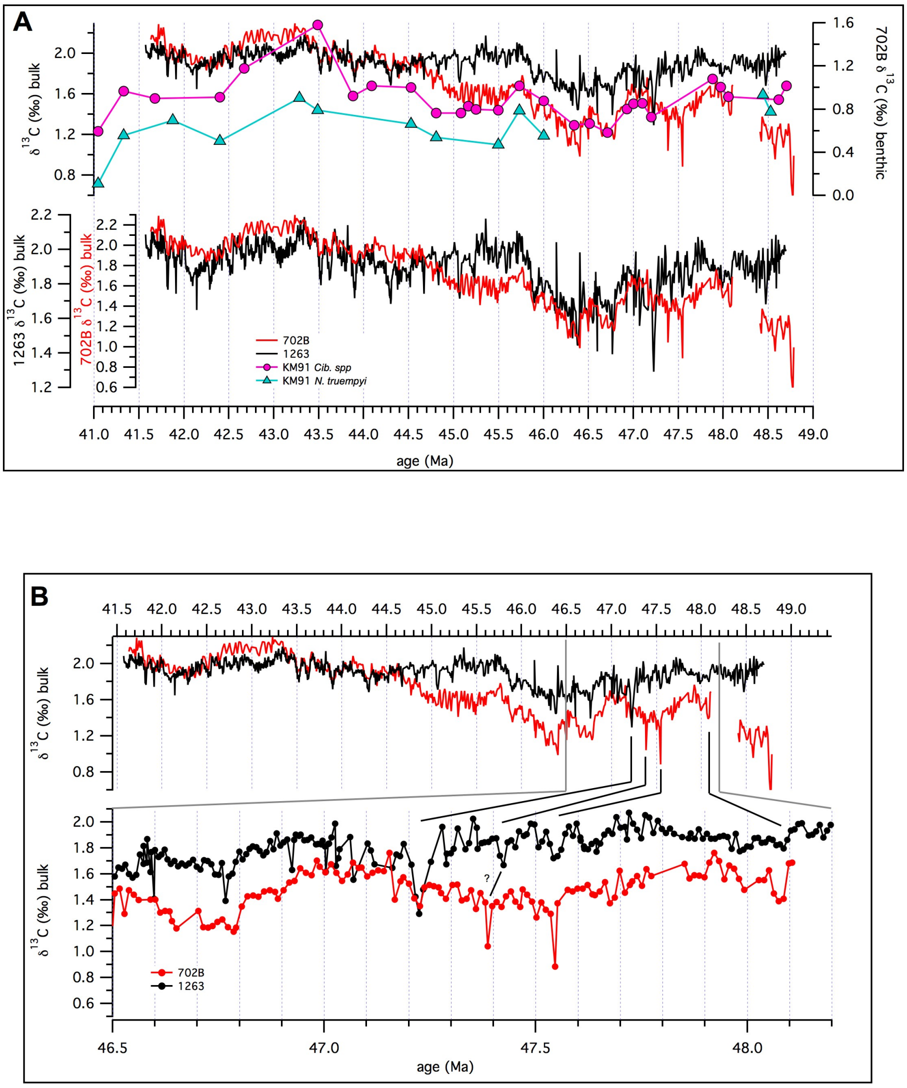

A
B
δ13C (‰) bulk
702B δ13C (‰) benthic
1263 δ13C (‰) bulk
702B δ13C (‰) bulk
702B
1263
KM91 Cib. spp
KM91 N. truempyi
age (Ma)

Figure S8

Dataset

Astronomical Calibration of the Geological Timescale: Closing the Middle Eocene Gap

Thomas Westerhold*, Ursula Röhl, Thomas Frederichs, Steve M. Bohaty, James C. Zachos

*email: twesterhold@marum.de

The data reported in this paper are open access archived at the Pangaea (www.pangaea.de) database online at http://doi.pangaea.de/10.1594/PANGAEA.845986. This supplement includes tables S4 to S13; extensive tables S1 to S3 are open access available at the links to Pangaea database.

Tables:

- Table S1 - Bulk stable isotope data ODP 702B (available here)
- Table S2 - Bulk stable isotope data ODP 1263 (available here)
- Table S3 – ODP 1263 raw inclination, declination, and intensity data for each measurement step (available here)
- Table S4 - Magnetostratigraphy ODP 1263
- Table S5 - Hole 702B and Site 1263 Calcareous Nannofossil datums
- Table S6 - Relative and absolute 405-kyr eccentricity cycle age model for ODP Hole 702B and Site 1263
- Table S7 - Offsets applied to cores from Holes 1263A, 1263B, 1263C
- Table S8 - List of tie points to create the revised composite depth scale (rmcd) for Site 1263
- Table S9 - Paleomagnetic data from ODP 1263
- Table S10 - Astronomical tuning age tie points
- Table S11 - Comparison of magnetochron boundary ages in million years
- Table S12 - Comparison of magnetochron boundary durations in million years
- Table S13 - Comparison of durations of magnetochrons in million years including uncertainties in magnetic anomaly width

Table S4 Magnetostratigraphy ODP 1263

Chron	Top			Bottom			Mean		
	Site, Hole, Core,	Depth		Site, Hole, Core,	Depth		Depth		Error
	Section, Interval (cm)	(mbsf)	(rmcd)	Section, Interval (cm)	(mbsf)	(rmcd)	(mbsf)	(rmcd)	(m)
C20n (y)	1263B-10H-4, 30	136.30	160.34	1263B-10H-4, 50	136.50	160.54	136.40	160.44	± 0.1
C20n (o)	1263B-11H-4, 141	146.91	171.94	1263B-11H-5, 11	147.11	172.14	147.01	172.04	± 0.1
C21n (y)	1263A-19H-5, 108	170.88	199.94	1263B-14H-1, 97	170.47	200.14	170.68	200.04	± 0.1
C21n (o)	1263B-15H-6, 99	185.49	216.34	1263B-15H-6, 39	185.89	216.74	185.69	216.54	± 0.2

Table S5 Hole 702B and Site 1263 Calcareous Nannofossil datums

Bioevent	Age§	Position in#	Top	Bottom	Top	Bottom	Mean	error
		Magneto-	Core, section	Core, section	Depth	Depth	Depth	
		stratigraphy	interval (cm)	interval (cm)	(m)	(m)	(m)	(±m)
Hole 702B*								
LO R. umbilicus >14µm	43.06	C20n.58	702B11X-5,5	702B11X-5,45	97.85	98.25	98.05	0.20
Site 1263**								
HO *Nannotetrina spp.*	43.06	C20n.58	1263A15H-CC	1263A16H-1,45	155.27	157.16	156.22	0.94
HO *N. fulgens (alata)*	43.72	C20n	1263A15H-CC	1263B11H-4,80	169.84	171.34	170.59	0.75
HO *C. gigas*	43.96	C20r.93	1263B12H-1,40	1263B12H-1,140	177.09	178.09	177.59	0.50
LO *C. gigas*	46.11	C20r.06	1263B13H-3,120	1263B13H-4,40	192.38	193.08	192.73	0.35
LO *N. fulgens (alata)*	46.80	C21n.68	1263B14H-3,40	1263B14H-3,120	202.58	203.39	202.99	0.40
HO *D. lodoensis*	48.37	C21r.59	1263A21H-2,40	1263A21H-2,140	215.04	215.56	215.06	0.26

Note: HO = highest occurence, LO = lowest occurence; §Agnini et al. 2014, *Pea 2011, **Shipboard Scientific Party 2004, #Position in Magnetochron is from Base of Chron; depth in 702B is mbsf and 1262 is rmcd.

Table S6 Relative and absolute 405-kyr eccentricity cycle age model for ODP Hole 702B and Site 1263

405-kyr	Site 702B	Site 1263	relative age	absolute age	
cycle	depth (mbsf)	depth (rmcd)	(Ma)	405-kyr cycle	La2011 (Ma)
# 1	-	158.60	0.405	# 104	41.904
# 2	-	161.25	0.810	# 105	42.308
# 3	-	165.10	1.215	# 106	42.708
# 4	108.20	168.70	1.620	# 107	43.112
# 5	115.20	172.20	2.025	# 108	43.516
# 6	121.60	175.50	2.430	# 109	43.928
# 7	128.00	178.90	2.835	# 110	44.336
# 8	133.80	183.00	3.240	# 111	44.740
# 9	-	186.70	3.645	# 112	45.140
# 10	148.20	(192.10)	4.050	# 113	45.540
# 11	154.40	197.20	4.455	# 114	45.948
# 12	161.60	202.40	4.860	# 115	46.360
# 13	168.50	207.10	5.265	# 116	46.768
# 14	175.30	211.70	5.670	# 117	47.176
# 15	183.00	216.30	6.075	# 118	47.572
# 16	189.70	220.90	6.480	# 119	47.972
# 17	195.30	225.70	6.885	# 120	48.372

Table S7 Offsets applied to cores from Holes 1263A, 1263B, 1263C

Core	Offset Ship (m)	Revised Offset (m)	Δ Ship – Revised (m)	Depth (mbsf)	Depth (rmcd)	Source
208-1263A-						
1H	0.00	0.00	0.00	0.00	0.00	ship
2H	0.41	0.41	0.00	2.30	2.71	ship
3H	2.12	2.12	0.00	11.80	13.92	ship
4H	3.83	3.83	0.00	21.30	25.13	ship
5H	3.85	3.85	0.00	30.80	34.65	ship
6H	7.25	7.25	0.00	40.30	47.55	ship
7H	9.11	9.06	0.05	49.80	58.86	this study
8H	10.71	10.11	0.60	59.30	69.41	this study
9H	11.77	11.14	0.63	68.80	79.94	this study
10H	11.79	11.29	0.50	78.30	89.59	this study
11H	13.17	12.67	0.50	87.80	100.47	this study
12H	13.73	13.23	0.50	97.30	110.53	this study
13H	17.53	17.03	0.50	106.80	123.83	this study
14H	17.75	21.03	-3.28	116.30	137.33	this study
15H	20.52	23.73	-3.21	125.80	149.53	this study
16H	21.89	25.13	-3.24	135.30	160.43	this study
17H	23.02	26.34	-3.32	144.80	171.14	this study
18H	23.94	27.44	-3.50	154.30	181.74	this study
19H	25.47	29.06	-3.59	163.80	192.86	this study
20H	27.77	31.36	-3.59	173.30	204.66	this study
21H	30.34	33.83	-3.49	182.80	216.63	this study
22H*	32.34	31.86	0.48	192.30	224.16	this study
23H	32.55	32.55	0.00	201.80	234.35	ship
24H	34.65	34.65	0.00	208.10	242.75	ship
25H	35.85	35.85	0.00	217.60	253.45	ship
26H	36.85	36.85	0.00	222.60	259.45	ship
27H	40.03	40.03	0.00	232.10	272.13	ship
28H	42.52	42.52	0.00	241.60	284.12	ship
29H	43.70	43.78	-0.08	251.10	294.88	W07
30H	45.71	45.79	-0.08	260.60	306.39	W07
31H	46.40	46.48	-0.08	270.10	316.58	W07
32H	48.38	49.08	-0.70	271.60	320.68	W07
33H	51.00	50.60	0.40	281.10	331.70	W07
34X	51.24	50.86	0.38	284.10	334.96	W07
35X	52.36	51.98	0.38	290.30	342.28	W07
36X	54.10	53.72	0.38	300.00	353.72	W07
37X	55.38	55.00	0.38	307.10	362.10	W07
38X	57.11	56.73	0.38	316.70	373.43	W07
39X	58.85	58.47	0.38	326.40	384.87	W07
40X	60.58	60.20	0.38	336.00	396.20	W07
208-1263B-						
1H	7.31	7.30	0.01	46.00	53.30	this study
2H	9.41	9.00	0.41	55.50	64.50	this study
3H	11.04	10.45	0.59	65.00	75.45	this study
4H	12.09	11.43	0.66	74.50	85.93	this study
5H	14.69	14.25	0.44	84.00	98.25	this study
6H	15.64	15.27	0.37	93.50	108.77	this study
7H	16.98	20.32	-3.34	103.00	123.32	this study
8H	18.34	21.57	-3.23	112.50	134.07	this study
9H	19.95	23.23	-3.28	122.00	145.23	this study
10H	20.78	24.04	-3.26	131.50	155.54	this study
11H	21.78	25.03	-3.25	141.00	166.03	this study
12H	22.68	26.20	-3.52	150.50	176.70	this study
13H	24.57	28.17	-3.60	160.00	188.17	this study
14H	26.12	29.67	-3.55	169.50	199.17	this study
15H	27.35	30.85	-3.50	177.00	207.85	this study
16H	29.69	33.13	-3.44	186.50	219.63	this study
17H*	29.69	29.21	0.48	196.00	225.21	this study
18H*	31.11	30.63	0.48	197.20	227.83	this study
19H	32.60	32.60	0.00	201.00	233.60	ship
20H	33.71	33.71	0.00	204.90	238.61	ship
21H	35.92	35.92	0.00	214.40	250.32	ship
22H	38.33	38.33	0.00	223.90	262.23	ship
23H	40.47	40.47	0.00	233.40	273.87	ship

24H	42.29	42.29	0.00	242.90	285.19	ship
25H	42.95	43.03	-0.08	252.40	295.43	W07
26X	44.12	44.20	-0.08	261.90	306.10	W07
27X	47.38	49.28	-1.90	271.10	320.38	W07
28X	50.83	50.58	0.25	280.70	331.28	W07
29X	52.56	52.16	0.40	290.30	342.46	W07
30X	54.30	53.90	0.40	300.00	353.90	W07
31X	56.03	55.63	0.40	309.60	365.23	W07
32X	57.76	57.36	0.40	319.20	376.56	W07
33X	59.51	59.11	0.40	328.90	388.01	W07
208-1263C-						
1H	13.11	12.72	0.39	90.00	102.72	this study
2H	14.98	17.5	-2.52	99.50	117.00	this study
3H	18.26	21.48	-3.22	109.00	130.48	this study
4H*	32.32	31.84	0.48	193.00	224.84	this study
5H	33.00	33.00	0.00	202.50	235.50	ship
6H	33.83	33.83	0.00	212.00	245.83	ship
7H	34.27	34.27	0.00	221.50	255.77	ship
8H	36.94	36.94	0.00	225.40	262.34	ship
9H	39.79	39.79	0.00	234.90	274.69	ship
10H	41.88	41.88	0.00	244.40	286.28	ship
11H	43.71	43.79	-0.08	253.90	297.69	W07
12H	45.42	45.5	-0.08	263.40	308.90	W07
13H	47.21	47.98	-0.77	272.90	320.88	W07
14H	50.31	49.91	0.40	282.40	332.31	W07
15H	50.31	49.91	0.40	285.60	335.51	W07
16X	50.83	51.08	-0.25	285.70	336.78	W07
208-1263D-						
1H	46.48	45.76	0.72	272.00	317.76	W07
2H	48.38	47.73	0.65	275.20	322.93	W07
3H	50.61	50.34	0.27	281.50	331.84	W07
4H	50.63	50.30	0.33	284.30	334.60	W07

* strong core disturbance

Table S8 List of tie points to create the revised composite depth scale (rmcd) for Site 1263

Hole, core, section interval (cm)	Depth (mbsf)	Depth (rmcd)		Hole, core, section interval (cm)	Depth (mbsf)	Depth (rmcd)	Source
1263A-1H-2, 50	2.00	2.00	Append to	1263A-2H-1, 0	2.30	2.71	ship
1263A-2H-7, 30	11.60	12.01	Append to	1263A-3H-1, 0	11.80	13.92	ship
1263A-3H-7, 30	21.10	23.22	Append to	1263A-4H-1, 0	21.30	25.13	ship
1263A-4H-7, 35	30.65	34.48	Tie to	1263A-6H-1, 0	40.30	47.55	ship
1263A-6H-5, 12.5	46.425	53.675	Tie to	1263B-1H-1, 37.5	46.375	53.675	this study
1263B-1H-6, 57.5	54.075	61.385	Tie to	1263A-7H-2, 102.5	52.325	61.385	this study
1263A-7H-5, 47.5	56.275	65.345	Tie to	1263B-2H-1, 85	56.35	65.345	this study
1263B-2H-5, 52.5	62.025	71.035	Tie to	1263A-8H-2, 12.5	60.925	71.035	this study
1263A-8H-6, 42.5	67.225	77.345	Tie to	1263B-3H-2, 40	66.90	77.345	this study
1263B-3H-5, 47.5	71.475	81.935	Tie to	1263A-9H-2, 50	70.80	81.935	this study
1263A-9H-7, 7.5	77.375	88.525	Tie to	1263B-4H-2, 110	77.10	88.525	this study
1263B-4H-6, 45	82.45	93.89	Tie to	1263A-10H-3, 130	82.60	93.89	this study
1263A-10H-7, 42.5	87.725	99.025	Tie to	1263B-5H-1, 77.5	84.775	99.025	this study
1263B-5H-7, 17.5	92.705	106.965	Tie to	1263C-1H-3, 125	94.25	106.965	this study
1263C-1H-6, 12.5	97.625	110.37	Tie to	1263B-6H-2, 10	95.10	110.37	this study
1263B-6H-6, 127.5	102.275	117.545	Tie to	1263C-2H-1, 55	100.05	117.545	this study
1263C-2H-7, 6	108.06	125.54	Tie to	1263B-7H-2, 72	105.22	125.54	this study
1263B-7H-6, 137.5	111.875	132.075	Tie to	1263C-3H-2, 10	110.60	132.075	this study
1263C-3H-4, 47.5	113.975	135.465	Tie to	1263B-8H-1, 140	113.90	135.465	this study
1263B-8H-4, 55	117.55	139.13	Tie to	1263A-14H-2, 30	118.10	139.13	this study
1263A-14H-6, 150	123.89	144.93	Append to	1263B-9H-1, 0	122.00	145.23	this study
1263B-9H-4, 115	127.65	150.88	Tie to	1263A-15H-1, 135	127.15	150.88	this study
1263A-15H-5, 40	132.20	155.94	Tie to	1263B-10H-1, 40	131.90	155.94	this study
1263B-10H-5, 30	137.80	161.85	Tie to	1263A-16H-1, 142.5	136.725	161.85	this study
1263A-16H-6, 17.5	142.975	168.105	Tie to	1263B-11H-2, 57.5	143.075	168.105	this study
1263B-11H-6, 75	149.25	174.29	Tie to	1263A-17H-3, 15	147.95	174.29	this study
1263A-17H-6, 15	152.45	178.80	Tie to	1263B-12H-2, 60	152.60	178.80	this study
1263B-12H-6, 80	157.50	183.71	Tie to	1263A-18H-2, 47.5	156.275	183.71	this study
1263A-18H-5, 102.5	161.325	188.765	Tie to	1263B-13H-1, 60	160.60	188.765	this study
1263B-13H-4, 132.5	165.825	194.005	Tie to	1263A-19H-1, 115	164.95	194.005	this study
1263A-19H-5, 102.5	170.825	199.895	Tie to	1263B-14H-1, 72.5	170.225	199.895	this study
1263B-14H-5, 137.5	176.875	206.555	Tie to	1263A-20H-2, 40	175.20	206.555	this study
1263A-20H-5, 70	180.00	211.37	Tie to	1263B-15H-3, 52.5	180.525	211.37	this study
1263B-15H-7, 5	186.05	216.90	Tie to	1263A-21H-1, 27.5	183.075	216.90	this study
1263A-21H-3, 97.5	186.775	220.605	Tie to	1263B-16H-1, 97.5	187.475	220.605	this study
1263B-16H-7, 57.5	196.075	229.215	**strong coring disturbance from 229.22 to 233.60**				
				1263B-19H-1	201.00	233.60	W07
1263B-19H-3, 8	204.08	236.68	Tie to	1263A-23H-2, 83.5	204.13	236.68	W07
1263A-23H-4, 48	206.76	239.31	Tie to	1263B-20H-1, 70	205.60	239.31	W07
1263B-20H-7, 33	214.22	247.93	Tie to	1263A-24H-4, 67.5	213.28	247.93	W07
1263A-24H-7, 25	217.25	251.90	Tie to	1263B-21H-2, 7.5	215.98	251.90	W07
1263B-21H-5, 103	221.42	257.34	Tie to	1263C-7H-2, 11	223.07	257.34	W07
1263C-7H-4, 15	225.28	259.55	Tie to	1263A-26H-1, 10	222.70	259.55	W07
1263A-26H-3, 120	226.80	263.65	Tie to	1263B-22H-1, 142	225.32	263.65	W07
1263B-22H-7, 65	233.55	271.88	Append to	1263A-27H-1, 0	232.10	272.13	W07
1263A-27H-6, 55	240.15	280.18	Tie to	1263C-9H-4, 98.5	240.39	280.18	W07
1263C-9H-7, 65	244.55	284.34	Tie to	1263A-28H-1, 22.5	241.82	284.34	W07
1263A-28H-3, 78	245.38	287.90	Tie to	1263B-24H-2, 121	245.61	287.90	W07
1263B-24H-6, 20	250.60	292.89	Tie to	1263C-10H-5, 61	251.01	292.89	W07
1263C-10H-7, 122	254.12	296.00	Tie to	1263A-29H-1, 112	252.22	296.00	W07
1263A-29H-5, 120	258.30	302.00	Tie to	1263C-11H-3, 138.5	258.29	302.08	W07
1263C-11H-7, 5	263.35	307.06	Tie to	1263A-30H-1, 75	261.35	307.14	W07
1263A-30H-7, 33	269.92	315.63	Tie to	1263C-12H-5, 81	270.21	315.71	W07
1263C-12H-CC, 28	273.09	318.59	Tie to	1263D-1H-1, 82.5	272.825	318.585	W07
1263D-1H-2, 115	274.65	320.41	Tie to	1263B-27X-1, 3	271.13	320.41	W07
1263B-27X-1, 145	272.55	321.83	Tie to	1263A-32H-1, 115	272.75	321.83	W07
1263A-32H-5, 30	277.90	326.98	Tie to	1263C-13H-5, 10	279.00	326.98	W07
1263C-13H-cc, 10	282.87	330.77	Append to	1263D-3H-1, 0.0	281.50	331.84	R07
1263D-3H-1, 90	282.40	332.74	Tie to	1263C-14H-1, 43	282.83	332.74	R07
1263C-14H-2, 149	285.39	335.30	Tie to	1263D-4H-1, 70	285.00	335.30	R07
1263D-4H-1, 90	285.20	335.50	Tie to	1263A-34X-1, 54	284.64	335.50	R07
1263A-34X-2, 146	287.06	337.92	Tie to	1263C-16X-1, 114	286.84	337.92	R07
1263C-16X-3, 60	288.80	339.88	end of splice				

Table S9 Paleomagnetic data interpretation from ODP 1263

Site	Hole	Core Type	Section	Section depth (cm)	Depth mbsf	Depth rmcd	Inclination (°)	Declination (°)	MAD (°)	steps used
1263	A	15H	4	91	131.21	154.94	61.9	245.7	3.3	2,3,4,5,6,7,8
1263	B	10H	1	40	131.90	155.94	42.4	159.5	5.9	2,3,4,5,6,7,8
1263	B	10H	1	140	132.90	156.94	52.1	75.2	3.8	2,3,4,5,6,7
1263	B	10H	2	90	133.90	157.94	3.8	11.3	7.1	2,3,4,5,6
1263	B	10H	3	40	134.90	158.94	48.1	32.9	5.0	2,3,4,5,6,7,8
1263	B	10H	3	140	135.90	159.94	80.2	93.3	3.3	2,3,4,5,6
1263	B	10H	4	10	136.10	160.14	56.3	307.5	2.5	2,3,4,5,6,7
1263	B	10H	4	30	136.30	160.34	65.3	43.6	4.2	2,3,4,5,6,7
1263	B	10H	4	50	136.50	160.54	-48.7	279.4	8.4	2,3,4,5,6
1263	B	10H	4	70	136.70	160.74	-64.0	224.3	4.0	2,3,4,5,6,7,8
1263	B	10H	4	90	136.90	160.94	-80.8	272.7	5.2	2,3,4,5,6,7
1263	B	10H	5	40	137.90	161.94	-49.3	223.9	4.9	2,3,4,5,6,7,8
1263	A	16H	2	101	137.81	162.94	-42.4	112.1	5.4	2,3,4,5,6,7,8
1263	A	16H	3	51	138.81	163.94	-37.0	170.3	2.6	2,3,4,5,6,7,8
1263	A	16H	4	1	139.81	164.94	-9.8	160.5	3.1	2,3,4,5,6,7,8
1263	A	16H	4	101	140.81	165.94	-20.8	114.9	5.5	2,3,4,5,6
1263	A	16H	5	51	141.81	166.94	-45.0	155.8	3.0	2,3,4,5,6,7,8
1263	A	16H	6	1	142.81	167.94	-29.2	159.8	2.0	2,3,4,5,6,7,8
1263	B	11H	2	141	143.91	168.94	-20.7	245.0	3.7	2,3,4,5,6
1263	B	11H	3	91	144.91	169.94	-24.4	247.1	4.0	2,3,4,5,6,7
1263	B	11H	4	41	145.91	170.94	-35.8	212.7	1.7	2,3,4,5,6,7,8
1263	B	11H	4	141	146.91	171.94	-46.2	161.1	5.0	3,4,5,6,7,8
1263	B	11H	5	11	147.11	172.14	37.0	189.3	5.8	2,3,4,5,6
1263	B	11H	5	31	147.31	172.34	27.5	259.2	4.7	3,4,5,6
1263	B	11H	5	51	147.51	172.54	66.6	269.7	4.2	2,3,4,5,6,7
1263	B	11H	5	71	147.71	172.74	-4.7	213.8	5.6	2,3,4,5,6,7
1263	B	11H	5	91	147.91	172.94	71.0	134.7	2.1	3,4,5,6,7
1263	B	11H	6	41	148.91	173.94	54.2	117.2	7.2	2,3,4,5,6
1263	A	17H	3	80	148.60	174.94	-56.9	3.2	6.7	2,3,4
1263	A	17H	4	30	149.60	175.94	64.8	341.3	3.4	2,3,4,5,6
1263	A	17H	4	130	150.60	176.94	70.8	312.5	3.5	2,3,4,5,6,7,8
1263	A	17H	5	80	151.60	177.94	16.3	315.3	5.0	2,3,4,5,6
1263	B	12H	2	74	152.74	178.94	-14.7	296.4	5.1	4,5,6,7
1263	B	12H	3	24	153.74	179.94	45.8	23.4	6.6	2,3,4,5,6
1263	B	12H	4	39	154.74	180.94	14.3	313.8	3.7	2,3,4,5,6,7,8
1263	B	12H	5	54	155.74	181.94	-9.3	53.9	1.6	4,5,6,7,
1263	B	12H	6	4	156.74	182.94	12.8	295.3	1.5	2,3,4,5,6,7,8,
1263	A	18H	2	70	180.44	183.94	86.5	228.4	4.4	2,3,4,5,6,7,8,
1263	A	18H	3	20	181.44	184.94	79.6	140.7	3.5	2,3,4,5,6,7,8,
1263	A	18H	3	120	182.44	185.94	53.2	145.5	2.5	2,3,4,5,6,7,
1263	A	18H	4	70	183.44	186.94	73.0	51.2	3.7	2,3,4,5,6,7,8,
1263	A	18H	5	20	184.44	187.94	72.8	122.2	2.4	2,3,4,5,6,7,8,
1263	B	13H	1	77	160.77	188.94	82.6	339.8	2.3	2,3,4,5,6,7,8,
1263	B	13H	2	27	161.77	189.94	62.9	131.6	2.6	2,3,4,5,6,7,
1263	B	13H	2	127	162.77	190.94	44.0	147.8	5.5	2,3,4,5,6,7,
1263	B	13H	3	77	163.77	191.94	47.8	121.9	2.3	2,3,4,5,6,7,8,
1263	B	13H	4	27	164.77	192.94	49.2	146.5	5.5	3,4,5,6,7,
1263	B	13H	4	127	165.77	193.94	69.4	253.3	6.6	2,3,4,5,6,7,
1263	A	19H	2	58	165.88	194.94	29.7	225.4	4.3	2,3,4,5,6,
1263	A	19H	3	8	166.88	195.94	53.4	296.0	3.7	2,3,4,5,6,7,8,
1263	A	19H	3	108	167.88	196.94	49.1	141.1	4.8	3,4,5,6,
1263	A	19H	4	58	168.88	197.94	28.1	159.4	4.1	2,3,4,5,6,7,8,
1263	A	19H	5	8	169.88	198.94	47.5	321.9	4.6	2,3,4,5,6,
1263	A	19H	5	108	170.88	199.94	35.4	355.1	3.8	2,3,4,5,
1263	B	14H	1	77	170.27	199.94	39.6	305.4	3.8	2,3,4,5,
1263	B	14H	1	97	170.47	200.14	-43.5	259.1	6.0	2,3,4,5,6,7,8
1263	B	14H	1	117	170.67	200.34	-22.4	238.1	8.9	3,4,5,6
1263	B	14H	1	137	170.87	200.54	-9.4	279.2	5.3	4,5,6
1263	B	14H	2	7	171.02	200.74	-29.7	259.5	5.4	2,3,4,5,6
1263	B	14H	2	27	171.26	200.94	-28.6	249.0	8.1	4,5,6
1263	B	14H	2	47	171.47	201.14	-82.1	270.8	1.5	2,3,4,5,6
1263	B	14H	2	127	172.27	201.94	-67.0	300.2	5.1	3,4,5,6,7
1263	B	14H	3	77	173.27	202.94	23.8	305.1	6.3	2,3,4,5,6,7,8
1263	B	14H	4	27	174.27	203.94	-57.7	301.9	3.5	2,3,4,5,6
1263	B	14H	4	127	175.27	204.94	-32.9	344.6	5.9	4,5,6,7
1263	B	14H	5	77	176.27	205.94	-74.0	315.8	3.4	4,5,6,7,8
1263	A	20H	2	78	175.58	206.94	-18.0	238.8	1.8	2,3,4,5,6,7

1263	A	20H	3	28	176.58	207.94	10.3	212.4	7.4	2,3,4,5,6
1263	A	20H	3	128	177.58	208.94	-0.4	256.3	2.4	4,5,6,7
1263	A	20H	4	78	178.58	209.94	8.7	238.2	2.4	2,3,4,5,6,7,8
1263	B	15H	3	20	180.20	211.05	-40.4	143.9	2.7	2,3,4,5,6,7,8
1263	B	15H	3	109	181.09	211.94	-8.7	124.4	2.0	2,3,4,5,6,7,8
1263	B	15H	4	59	182.09	212.94	-18.5	216.9	6.4	2,3,4,5,6,7
1263	B	15H	5	9	183.09	213.94	-15.7	147.0	3.8	2,3,4,5,6,7,8
1263	B	15H	5	109	184.09	214.94	-36.7	146.0	3.8	2,3,4,5,6,7,8
1263	B	15H	6	39	184.89	215.74	-46.0	169.5	1.1	2,3,4,5,6,7,8
1263	B	15H	6	59	185.09	215.94	-44.8	158.5	4.7	2,3,4,5,6,7,8
1263	B	15H	6	79	185.29	216.14	-36.7	158.3	2.2	2,3,4,5,6,7,8
1263	B	15H	6	99	185.49	216.34	-12.0	155.1	2.7	3,4,5,6,7
1263	B	15H	6	119	185.69	216.54	-6.9	147.6	2.1	3,4,5,6
1263	B	15H	6	139	185.89	216.74	16.5	170.6	3.6	2,3,4,5,6
1263	B	15H	7	9	186.09	216.94	5.7	169.8	1.2	4,5,6,7
1263	A	21H	1	31	183.11	216.94	11.9	260.4	2.3	2,3,4,5,6
1263	B	15H	7	29	186.29	217.14	-25.3	145.5	4.5	2,3,4,5,6
1263	B	15H	7	49	186.49	217.34	-12.7	148.6	6.1	2,3,4,5,6,7
1263	A	21H	1	131	184.11	217.94	46.6	251.3	3.1	2,3,4,5,6,7
1263	A	21H	2	81	185.11	218.94	10.0	1.0	2.7	2,3,4,5
1263	A	21H	3	31	186.11	219.94	2.5	272.8	3.1	3,4,5,6,7
1263	A	21H	3	131	187.11	220.94	70.8	203.5	4.5	2,3,4,5,6,7
1263	A	21H	4	81	188.11	221.94	52.3	37.0	2.6	3,4,5
1263	A	21H	5	31	189.11	222.94	12.0	274.6	2.1	3,4,5,6,7,8
1263	A	21H	5	131	190.11	223.94	57.3	2.8	3.8	2,3,4,5,6
1263	A	21H	6	81	191.11	224.94	63.9	87.7	9.0	2,3,4,5
1263	B	16H	5	31	192.81	225.94	32.0	15.5	8.4	2,3,4,5,6,7,8
1263	B	16H	5	131	193.81	226.94	66.1	62.1	3.1	2,3,4,5,6,7
1263	B	16H	6	15	194.15	227.28	-1.6	153.2	4.9	3,4,5,6,7
1263	B	16H	6	50	194.50	227.63	-9.2	191.4	5.5	4,5,6,7
1263	B	16H	6	81	194.81	227.94	-49.0	168.0	6.2	3,4,5
1263	B	16H	6	137	195.37	228.50	-35.2	192.0	6.8	3,4,5,6,7
1263	B	16H	7	35	195.85	228.98	3.7	0.9	9.0	3,4,5,6

Table S10 Astronomical tuning age tie points

ODP 1263		ODP 702B	
depth (rmcd)	Age La2011 (Ma)	depth (mbsf)	Age La2011 (Ma)
150.69	40.945968	91.69	41.621043
152.14	41.136030	94.92	41.818290
158.17	41.816454	98.23	42.083093
161.86	42.287809	103.22	42.513360
164.64	42.679338	112.04	43.344957
168.04	43.063264	115.02	43.522767
172.93	43.618246	116.70	43.619268
175.41	43.895737	121.26	43.894984
178.85	44.294868	126.92	44.293018
186.25	45.161553	133.80	44.740000
192.10	45.540000	148.20	45.540000
197.23	45.895194	154.36	45.898210
202.53	46.377953	162.16	46.381028
207.07	46.761879	168.83	46.757840
211.77	47.142004	175.94	47.225596
217.13	47.628564	181.74	47.545265
220.76	47.981547	190.89	48.082781
226.47	48.472441		

Table S11 Comparison of magnetochron boundary ages in million years

Chron	standard GPTS			tuned		tuned – this study[†]			
	CK95	GPTS 2004	GPTS 2012	PEAT Sites[#]	Contessa Hyw	ODP Site 1260	ODP Site 1258 opt.2	ODP Site 1263	ODP Site 702B
C18n.2n (o)	40.130	39.464	40.145	40.076 ± 5	40.120				
C19n (y)	41.257	40.439	41.154	*41.075 ± 7*	41.250	41.061 ± 9		41.030 ± 13	
C19n (o)	41.521	40.671	41.390	*41.306 ± 5*	41.510	41.261 ± 4		41.180 ± 11	
C20n (y)	42.536	41.590	42.301	*42.188 ± 15*	42.540	42.152 ± 7		42.107 ± 13	42.124 ± 4
C20n (o)	43.789	42.774	43.432		43.790	43.449 ± 18		43.517 ± 11	43.426 ± 3
C21n (y)	46.264	45.346	45.724		46.310			46.151 ± 9	46.080 ± 3
C21n (o)	47.906	47.235	47.349				47.723 ± 118	47.575 ± 18	
C22n (y)	49.037	48.599	48.566				48.954 ± 16		
C22n (o)	49.714	49.427	49.344				49.593 ± 42		
C23n.1n (y)	50.778	50.730	50.628				51.051 ± 21		
C23n.1n (o)	50.946	50.932	50.835				51.273 ± 39		
C23n.2n (y)	51.047	51.057	50.961				51.344 ± 32		
C23n.2n (o)	51.743	51.901	51.833				51.721 ± 23		
C24n.1n (y)	52.364	52.648	52.620				52.525 ± 23		
C24n.1n (o)	52.663	53.004	53.074				52.915 ± 29		
C24n.2n (y)	52.757	53.116	53.199				53.037		
C24n.2n (o)	52.801	53.167	53.274				53.111		
C24n.3n (y)	52.903	53.286	53.416				53.249 ± 17		
C24n.3n (o)	53.347	53.808	53.983				53.806 ± 20		

[†] tuned to the orbital solution La2011 (Laskar et al. 2011)
[#] combined ages based on Pacific Equatorial Age Transect Sites 1218, U1333 and U1334 (Westerhold et al. 2014)

Table S12 Comparison of magnetochron boundary durations in million years

Chron	standard GPTS			tuned		tuned – this study[†]			
	CK95	GPTS 2004	GPTS 2012	PEAT Sites[#]	Contessa Hyw	ODP Site 1260	ODP Site 1258 opt.2	ODP Site 1263	ODP Site 702B
C18n.2r	1.127	0.975	1.009	0.999 ± 12					
C19n	0.264	0.232	0.236	0.231 ± 12	0.260	0.200 ± 7		0.150 ± 24	
C19r	1.015	0.919	0.911	0.882 ± 20	1.030	0.891 ± 6		0.927 ± 24	
C20n	1.253	1.184	1.131		1.250	1.297 ± 13		1.410 ± 24	1.302 ± 7
C20r	2.475	2.572	2.292		2.520			2.634 ± 20	2.654 ± 6
C21n	1.642	1.889	1.625					1.424 ± 27	
C21r	1.131	1.364	1.217				1.231 ± 134		
C22n	0.677	0.828	0.778				0.639 ± 58		
C22r	1.064	1.303	1.284				1.458 ± 63		
C23n.1n	0.168	0.202	0.207				0.222 ± 60		
C23n.1r	0.101	0.125	0.126				0.071 ± 71		
C23n.2n	0.696	0.844	0.872				0.377 ± 55		
C23n.2r	0.621	0.747	0.787				0.804 ± 46		
C24n.1n	0.299	0.356	0.454				0.390 ± 52		
C24n.1r	0.094	0.112	0.125				0.122		
C24n.2n	0.044	0.051	0.075				0.074		
C24n.2r	0.102	0.119	0.142				0.138		
C24n.3n	0.444	0.522	0.567				0.557 ± 37		

[†] tuned to the orbital solution La2011 (Laskar et al. 2011)
[#] combined ages based on Pacific Equatorial Age Transect Sites 1218, U1333 and U1334 (Westerhold et al. 2014)

Table S13. Comparison of durations of magnetochrons in million years including uncertainties in magnetic anomaly width

Chron	CK95		GPTS2004		GPTS2012		this study		Source Site
	min	max	min	max	min	max	min	max	
C19	1.197	1.360	1.069	1.232	1.066	1.228	1.074	1.106	ODP 1260[*]
C20n	1.172	1.334	1.103	1.266	1.050	1.212	1.273	1.323	ODP 1260[*]
C20r	2.324	2.626	2.420	2.723	2.141	2.443	2.675	2.729	ODP 1260[*], 1263[#]
C21n	1.506	1.778	1.753	2.026	1.489	1.761	1.397	1.451	ODP 1263[#]
C21r	0.975	1.287	1.209	1.520	1.061	1.373	1.345	1.413	ODP 1258[§]
C22n	0.615	0.739	0.765	0.890	0.716	0.840	0.581	0.697	ODP 1258[§]
C22r	0.911	1.217	1.150	1.456	1.131	1.437	1.395	1.521	ODP 1258[§]
C23	1.241	1.931	1.574	2.263	1.647	2.337	1.430	1.518	ODP 1258[§]
C24	3.119	3.961	3.596	4.438	4.060	4.902	4.492	4.558	ODP 1258[§], 1262[**]

[*]Westerhold & Röhl (2013); [#]this study; [§]Westerhold & Röhl (2009), [**]Westerhold et al. (2007; option 2)
Note: minimum and maximum durations for CK95, GPTS2004 and GPTS2012 are based on the error given for the mean width of magnetic anomalies as published in table 4 of Cande & Kent (1992)